

1-1-2015

Adhesion of Germanium Electrode on Nickel Substrate for Lithium Ion Battery Applications

Aadithya Jeyaranjan

University of South Florida, aadithya916@gmail.com

Follow this and additional works at: <http://scholarcommons.usf.edu/etd>



Part of the [Materials Science and Engineering Commons](#)

Scholar Commons Citation

Jeyaranjan, Aadithya, "Adhesion of Germanium Electrode on Nickel Substrate for Lithium Ion Battery Applications" (2015). *Graduate Theses and Dissertations*.

<http://scholarcommons.usf.edu/etd/5509>

This Thesis is brought to you for free and open access by the Graduate School at Scholar Commons. It has been accepted for inclusion in Graduate Theses and Dissertations by an authorized administrator of Scholar Commons. For more information, please contact scholarcommons@usf.edu.

Adhesion of Germanium Electrode on Nickel Substrate for Lithium Ion Battery Applications

by

Aadithya Jeyaranajn

A thesis submitted in partial fulfillment
of the requirements for the degree of
Master of Science in Materials Science and Engineering
Department of Chemical and Biomedical Engineering
College of Engineering
University of South Florida

Major Professor: Alex Volinsky, Ph.D.
Wenjun Cai, Ph.D.
Ashok Kumar, Ph.D.

Date of Approval:
March 23, 2015

Keywords: Nanoindentation, Brittle Coatings on Ductile Substrate, Ion Beam Mixing, Irradiated
Materials, Interfacial Toughness

Copyright © 2015, Aadithya Jeyaranjan

DEDICATION

For my family and friends who stood by me during this two years journey and supported me through their never-ending patience and love.

ACKNOWLEDGMENT

I would like to start by thanking my thesis guide, Dr. Alex Volinsky without whose constant support this thesis would not have been possible. I thank him for his endless patience in clarifying my questions and his continuous encouragement to ask more questions without any hesitation.

I would like to express my sincere gratitude to my thesis committee members, Dr. Wenjun Cai and Dr. Ashok Kumar for spending their valuable time in helping me complete my Thesis. I would also like to thank all the faculty and staff of University of South Florida, Tampa for their constant support, which increased the confidence I had in myself.

I would also like to thank Dr. Kevin Jones and Dr. Nicholas Rudawski from University of Florida, Gainesville for providing me with the samples that served to be the starting point of my Thesis.

Finally, I would like to thank the Department of Mechanical Engineering at the University of South Florida, Tampa for providing me with the necessary laboratory facilities for carrying out my Thesis research.

Thank you all for making this a thoroughly enjoyable venture.

TABLE OF CONTENTS

LIST OF TABLES.....	iii
LIST OF FIGURES	iv
ABSTRACT.....	vi
CHAPTER 1: INTRODUCTION TO LI ION BATTERY TECHNOLOGY	1
1.1 Overview of Modern Battery Technology.....	1
1.2 The Li Ion Battery.....	2
1.3 The Need for Improved Batteries	3
1.3.1 Factors Affecting the Performance of Li Ion Batteries.....	3
1.3.2 Problems with the Original Anodes.....	4
1.3.3 Solution for Decrepitation.....	5
1.4 Formation of Nanopores in Ge	7
1.5 Nanopores Formation Theories.....	8
1.5.1 The Vacancy Clustering Theory	8
1.5.2 The Micro-Explosion Theory	9
1.6 Factors Affecting the Nanopore Formation	10
1.7 Electrochemical Cycling of the Ge Anode	12
CHAPTER 2: SELECTED RESULTS FROM FRACTURE AND CONTACT MECHANICS	16
2.1 Thin Film Adhesion	16
2.1.1 The Surface Energy.....	17
2.1.2 The Contact Angle	17
2.1.3 Practical Work of Adhesion.....	18
2.2 Fracture Mechanics Approach	19
2.2.1 Griffith Energy Balance.....	20
2.2.2 The Dundurs' Parameters	21
2.2.3 Stress Intensity Factor.....	22
2.2.4 The Phase Angle	24
2.3 Contact Mechanics.....	27
2.4 Load-Displacement Curves.....	29
2.5 Expanding Cavity Model	32
2.6 Pile-up and Sink-in	33

CHAPTER 3: THEORIES OF ADHESION MEASUREMENT AND RESIDUAL STRESSES.....	35
3.1 Thin Film Adhesion Measurement Techniques.....	35
3.1.1 Four-point Bending.....	35
3.1.2 The Superlayer Test.....	36
3.1.3 One-dimensional Buckling.....	39
3.1.4 Nanoindentation Test for Fracture.....	40
3.1.5 The Superlayer Indentation Test.....	42
3.1.6 Microwedge Indentation Test.....	43
3.1.7 The Drory and Hutchinson Model.....	45
3.2 Stresses in Thin Films.....	47
3.3 Residual Stress Measurements.....	48
CHAPTER 4: ADHESION MEASUREMENT AND DISCUSSIONS.....	50
4.1 Adhesion Measurements.....	50
4.2 Fabrication of the Test Specimens.....	50
4.3 Load Range Selection.....	51
4.4 Analysis of the Test Data.....	54
4.4.1 Qualitative Analysis.....	54
4.4.2 Quantitative Analysis.....	57
CHAPTER 5: SUMMARY AND FUTURE WORKS.....	63
5.1 Summary.....	63
5.2 Suggestions and Future Work.....	64
5.2.1 Surface Roughness.....	64
5.2.2 Effect of the Ion Dose.....	64
5.2.3 Plane Strain Indentation.....	64
5.2.4 Environmental Considerations.....	64
REFERENCES.....	66
APPENDIX A COPYRIGHT PERMISSIONS.....	72

LIST OF TABLES

Table 1.	Strain energy release rate values of the irradiated and non-irradiated samples with W superlayer.	58
Table 2.	Range of delamination radius.	61
Table 3.	Strain energy release rate for irradiated and non-irradiated samples.	61

LIST OF FIGURES

Figure 1. Li ion battery schematics for: a) charging and b) discharging.....	2
Figure 2. HR-XTEM images of a) the non-irradiated sample and b) the irradiated sample with superimposed Ge ion concentration profile.....	12
Figure 3. Electrochemical behavior of the Ge electrodes.	14
Figure 4. Schematics of a) interface crack and b) through-thickness crack.....	15
Figure 5. Two phases in equilibrium contact with each other and <i>in vacuo</i>	16
Figure 6. Surface energy and the contact angle.....	17
Figure 7. Modes of fracture.....	23
Figure 8. Interface energy as a function of phase angle.....	25
Figure 9. Indentation schematic of a conical indenter.....	29
Figure 10. A sample load-displacement curve.	31
Figure 11. Schematic of the expanding core model.	33
Figure 12. Schematic of a four-point bend test specimen.	36
Figure 13. Schematic of a superlayer test.....	38
Figure 14. Hypothetical steps used for strain energy calculation.....	42
Figure 15. Stresses in a superlayer indentation test specimen.	43
Figure 16. Schematic of the micro-wedge indentation test.....	44
Figure 17. Types of delamination.....	47
Figure 18. Schematics indentation test and the superlayer indentation test specimens.	51
Figure 19. Load-displacement curves for the non-irradiated sample without superlayer.....	52

Figure 20. Spacing between each indent and each set of indents.	53
Figure 21. Schematic of delamination measurement.	53
Figure 22. Delaminations observed in non-irradiated and irradiated samples.	54
Figure 23. Pop-in observed in non-irradiated samples without the superlayer.	55
Figure 24. Pop-in observed in non-irradiated samples with W the superlayer.	56
Figure 25. G vs. X/a values for a) as-is and b) irradiated samples with no W superlayer.	60
Figure 26. G vs. X/a values for a) as-is and b) irradiated samples with the W superlayer.	60

ABSTRACT

Lithium ion batteries (LIBs) have gained increasing popularity due to their high potential, low self-discharge, zero priming and minimal memory effect. However, the emergence of electrical vehicles and hybrid electrical vehicles in the automobile industry, where LIBs are predominantly in use, instilled a need to improve LIB batteries by experimenting with new materials. Graphite, the commonly used anode material for LIBs suffers from low theoretical capacity (372 mA h g^{-1}) and torpid rate performance. Germanium (Ge) seems to be a promising substitute of carbon due to its high theoretical capacity, high Li^+ diffusivity and electrical conductivity. However, Ge undergoes large volumetric change ($\pm 370\%$). This causes debonding of the thin film Ge electrode from the substrate current collector, causing a rapid decrease in the electrolytic performance. The process of ion beam mixing claims to have overcome this problem. In our current study, the adhesion strength of Ge thin film over Nickel (Ni) substrate (with and without ion beam mixing) is being measured using nanoindentation and the superlayer indentation test. Nanoindentation is one of the popular techniques to measure the mechanical properties and adhesion of thin film coatings. In this technique, a very small indenter of a desired geometry indents the film/substrate pair and the work of adhesion is calculated by knowing the plastic depth of indentation and the radius of indentation. Superlayer indentation is analogous to normal indentation but with a highly stressed superlayer on top to restrict the out-of-plane displacements, it reduces the plastic pile up around the indenter tip. The results from our study strongly suggest the possibility of dramatically increasing the adhesion strength by ion

bombardment, which can be achieved by atomic level intermixing of the film/substrate pair. These, in turn, suggest that Ge could be an effective successor to graphite in the near future.

CHAPTER 1:

INTRODUCTION TO LI ION BATTERY TECHNOLOGY

1.1 Overview of Modern Battery Technology

A battery consists of a single cell or multiple cells connected together in series or in parallel. The two primary functions of the battery are:

- 1) Energy storage;
- 2) Energy conversion (chemical to electrical energy and *vice versa*).

Based on rechargeability, batteries can be classified into two types, primary batteries and secondary batteries. Primary batteries are those that cannot be recharged and secondary batteries are those that can be recharged. The basic battery has an electrolyte and a pair of electrodes. The process of energy conversion is associated with charging and discharging cycles of the battery. The polarity of the electrodes in secondary batteries depends on the nature of operation of the battery. The anode has a negative polarity and the cathode, a positive polarity when battery supplies current to a system (discharge). The polarity of the electrodes flips when current is supplied to the battery (charge).

The primary battery, Zn-MnO₂ along with the secondary batteries of Ni and lead-acid batteries have been the three most commonly used batteries ever since the discovery of the first practical battery (the Volta cell) by Volta [1]. However, in the last two decades the scenario has changed with the advent of Li ion batteries. High potential, low self-discharge, zero priming and minimum memory effect has made Lithium ion batteries increasingly popular. In the recent

years, lithium ion batteries have been used in a wide range of applications, including laptops, cell phones, toys and automobiles [2-3].

1.2 The Li Ion Battery

Since Li is the lightest (0.53 g cm^{-3}) and the most electropositive metal (-3.04 V), the use of Li in power storage has given way to a lightweight battery with high power density [4]. Working cells with Li metal were demonstrated as early as 1970s. These initially developed Li metal batteries suffered from heating issues and other problems. Using Li ions instead of Li metal solved these problems (Li^+ redox potential of -3.01 V). Thus, Li metal batteries gave way for the Li ion batteries, which were first commercialized in 1990 [1].

The working of Li ion batteries is very similar to that of the Ni-MH batteries, which have H^+ ions as the intercalating species. Intercalation is the process by which the ions diffuse in and out of the electrodes. The associated ions are called intercalating species. During charging, Li ions move into the anode and during discharging, they move back into the cathode. Due to this back and forth motion of the ions, the battery is also called the rocking chair battery [5].

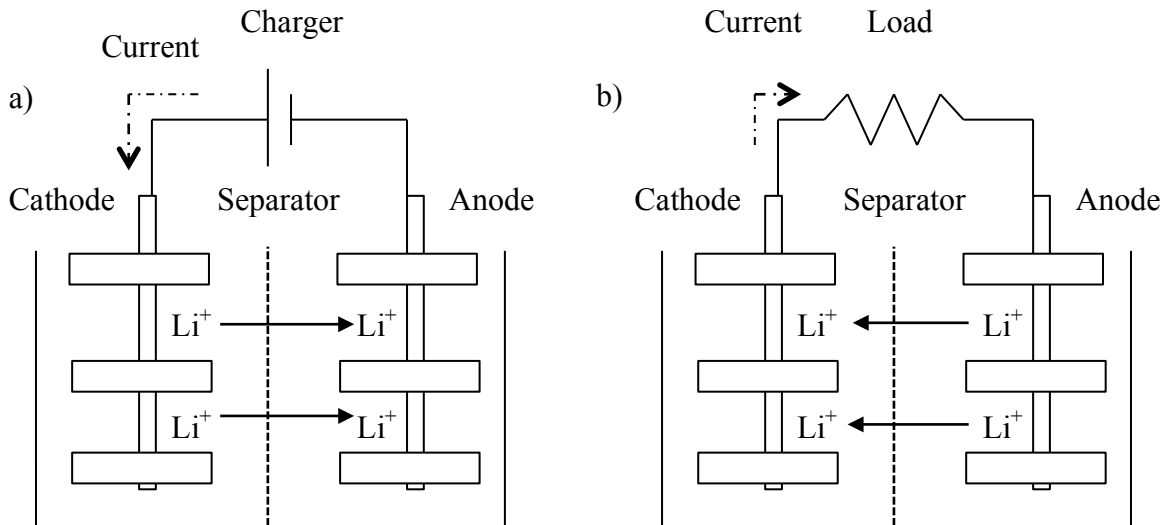


Figure 1. Li ion battery schematics for: a) charging and b) discharging.

The schematics of the working of a typical Li ion battery are shown in Figure 1. The general LIB consists of a Li metal oxide, such as lithium cobalt oxide LiCoO_2 as the cathode material, charcoal or graphite as the common anode material and a lithium salt in an organic solvent as electrolyte. The separator is usually made of thin micro-perforated plastic. Research on new electroactive materials have been done continuously for improved performance, higher safety and cheaper cost of the battery.

1.3 The Need for Improved Batteries

Moore's law [6] states that the number of transistors in integrated circuits doubles approximately every two years. This means that better batteries are constantly in need. One of the methods employed in improving the properties of batteries is finding new materials to replace the traditionally used battery materials.

1.3.1 Factors Affecting the Performance of Li Ion Batteries

A mathematical quasi 2D model of a Li-ion cell was developed by Chabot et al. [7]. The factors that dictate the performance of the battery are listed in descending order, based on computer simulations:

- 1) Li^+ ion diffusivity in the negative electrode.
- 2) Rate constant of the electrodes.
- 3) Li^+ ion diffusivity in the positive electrode.
- 4) Electrical conductivity of the anode and cathode.

Since the negative electrode has a huge impact on the performance of the battery, finding suitable anode material is one of the best methods to increase the performance of the Li ion battery.

1.3.2 Problems with the Original Anodes

The initial Li metal batteries, which used a Li metal anode suffered a loss in capacitance from the formation of dendrites at the surface of the electrodes due to electromigration [8]. When an electrode is made of a pure metal, a local positive charge is produced by the solute depletion near the surface of the electrode. This localized positive charge induces a faster rate of deposition of particles than the rest of the electrode surface, giving rise to projections on the electrode surface. These projections may grow into dendritic structures, whose orientation depends on the rate of deposition or the surface energy [9].

Organic electrolytes that have cationic groups become unstable when they come in contact with the highly negative potential electrodes. This interaction leads to the formation of reaction layers on the electrodes. These layers, known as solid electrode interphases (SEI), are ionic conductors in nature. Due to the discontinuities and defects in the SEI, dissimilarities in electrode electrical impedance were observed. This leads to irregular deposition rates. Higher rates of particle deposition were specifically observed at regions of higher current density. This phenomenon also leads to the formation of dendrite-like structures [10].

Over the course of time, these dendritic structures grow in size and give the electrodes a furry texture. At some point, these structures get cut off from the electrodes and cannot take part in the functioning of the battery. Such detached structures are termed as dead lithium [8].

There is also another problem associated with Li metal anodes. The decomposition of the unstable electrolyte during the formation of reaction product layers leads to the development of localized thermal issues in the batteries. The thermal runaway results in high temperatures close to the melting temperature of Li [11].

The problems associated with the use of Li metal electrodes lead to the usage of Li alloys as negative electrode. However, these alloys also suffered from a unique problem that caused a reduction in the capacity of the battery over time. Unlike the dendrite growth associated with pure Li metal electrodes, the capacitance loss was caused by a phenomenon known as decrepitation. Decrepitation is the process by which the alloy electrode fractures to minute particles due to the mechanical strains associated with electrochemical cycling. These smaller particles ultimately lose electrical contact with each other [8].

Huggins et al. [9] studied the decrepitation process using a 1D model and came up with the critical thickness below which fracture does not happen. This critical size is given by:

$$hc \approx \frac{23}{\pi} \left[\frac{K_{IC}}{B\varepsilon} \right]^2 \quad (1),$$

$$\varepsilon = \frac{e_T}{3} \quad e_T = \frac{\Delta V}{V}$$

where B is the biaxial stress, K_{IC} is mode I fracture toughness, ε is the misfit strain associated with thin films and e_T is the transformation strain.

1.3.3 Solution for Decrepitation

One of the challenges is that carbon has low capacity, thus there is a need of finding suitable replacements for carbon anodes, as carbon suffers from low theoretical capacity of 372 mA h g⁻¹ and torpid rate performance [4]. Other group IV elements have been considered as suitable replacements for graphite due to their high capacities (Si 4,200 mA h g⁻¹, Ge 1,600 mA h g⁻¹) and high Li ion diffusivity. Although the possibility of using Si as anode material has been studied in detail, the study of Ge electrodes started much later. Although, the group IV electrodes seem to be a very potential replacement for carbonaceous anodes, they suffer from a serious drawback. They undergo a large volumetric change (~400%) during the lithiation-delithiation

process [4, 12]. Such large-scale volume change causes enormous stresses, which leads to the pulverization of the electrode. This problem associated with large volume change can be solved by nanostructuring the electrodes (nanostructured thin film coatings).

The second Fick's law with the appropriate boundary conditions reduces to:

$$T = \frac{l^2}{D} \quad (2),$$

where l is the length of diffusion and D is the diffusion coefficient. It is clear from equation (2) that the stress relaxation is quicker by reducing the diffusion length. There are several other advantages of using nano-scale materials in Li ion batteries:

- 1) Increased charging and discharging rates because of the increased surfaced contact area;
- 2) Improved relaxation of the stresses that accompanies the charge/discharge cycle;
- 3) Decreased Li^+ transport length;
- 4) Better electrical contact between the electrode and the current collector.

The concept of increased surface area of the electrodes by using nanotechnology also has some disadvantages. The primary disadvantage is the unwanted interaction between the electrolyte and the electrodes, which produces a large number of side reactions. These side reactions lower the performance of the battery and cause the life span of the battery to reduce tremendously. Methods to suppress these side reactions were only realized in the last decade [3]. Thus, the use of nanotechnology in energy storage started rather late compared to other fields.

Graetz et al. [13] have shown that bulk materials of group IV elements, when used as electrodes, revealed a rapid decrease in capacity of the battery within a few cycles. Studies have shown that this fade in capacitance can be avoided by using nanoscale materials, like nanowires and nanoparticles for electrodes [14 - 15].

One such method is nanostructuring Ge by ion beam irradiation. The nanostructured Ge exhibits a superior electrical conductivity compared to amorphous and crystalline Ge. The Hall effect measurement by Impellizzeri et al. [16] has shown that the porous layer formed by self-implantation exhibited p-type conductivity.

Fuller et al. [17] studied the diffusion of Li into Ge and showed that diffusion curves followed an Arrhenius type equation. The diffusion constant, D , can be calculated as:

$$D = 25 \times 10^{-4} e^{\left(\frac{-11800}{Rt}\right)} \quad (3).$$

Laforge et al. [18] used galvanostatic intermittent titration technique and determined that the diffusion coefficient of Li into Ge varies in the range between $5 \times 10^{-12} \text{ cm}^2 \text{ s}^{-1}$ and $1.75 \times 10^{-10} \text{ cm}^2 \text{ s}^{-1}$, which is nearly two orders of magnitude higher than the diffusion coefficient of Li into Si that ranges between $2 \times 10^{-14} \text{ cm}^2 \text{ s}^{-1}$ and $10^{-13} \text{ cm}^2 \text{ s}^{-1}$.

1.4 Formation of Nanopores in Ge

Irradiation of crystalline Ge causes lattice displacement, thereby creating defects. Above a threshold limit, the irradiation exposure causes transition from crystalline to amorphous Ge. The evolution of nanopores is highly dependent on the dose of irradiation and temperature [19, 20]. This nanopore evolution process has four distinct process steps, as stated below:

- 1) When crystalline Ge is irradiated, there is an initial transformation from crystalline Ge (β -Ge) to amorphous Ge (α -Ge);
- 2) With the increase of the irradiation ion dose, pores start nucleating and clustering near the surface of the amorphous Ge layer;
- 3) The number of pores near the surface increases and the elongation of the pores is also observed with the ion dose increase;
- 4) Further increase in dose leads to additional elongation of the pores, which is followed by

the out-of-plane volumetric expansion. These nano-sized features are arranged over the amorphous layer.

The threshold dose for amorphization, void formation and nano-pore formation are $5 \times 10^{13} \text{ cm}^{-2}$, $2 \times 10^{15} \text{ cm}^{-2}$ and $4 \times 10^{15} \text{ cm}^{-2}$, respectively [19].

Although initial studies of nanostructuring of germanium were limited to using single crystal materials, latter studies have shown nanostructuring caused by irradiation of the polycrystalline or already amorphised Ge [21].

1.5 Nanopores Formation Theories

The irradiated particles produce elastic collision with the target atoms. The target atoms, which come in contact with the irradiated ions, are termed as the primary knock-on atoms (PKA). The cascading of many such PKAs produces ballistic waves with energies greater than the bonding energy of the lattice. The ballistic waves create lattice disturbances that are accompanied by localized thermal peaks. This phenomenon lasts only for a very short time as the energy rapidly falls below the threshold energy. By the end of this process, many Frenkel pairs are created, and the threshold energy for the production of Frenkel pairs in Ge is 15 eV [22].

1.5.1 The Vacancy Clustering Theory

Ion beam irradiation produces a large number of vacancies. According to molecular dynamics, vacancies are more stable and last for a longer time than interstitials. This difference in life times leads to the ineffective re-combination of the vacancies with interstitials. Pores are formed when the vacancies cluster together to maintain the minimum energy of the system. According to this theory, pore formation starts where the concentration of vacancies is the highest [20, 23 - 24].

1.5.2 The Micro-Explosion Theory

According to the micro-explosion theory, voids are formed by high-pressure waves generated by the continuous bombardment of ions. Only a very small fraction of the incident ions ($\sim 1/1000$), account for the critical energy, which is necessary to produce voids. This theory also states that the formation of the nanopores should always be near the surface and the formation of nanopores is independent of the temperature [25 - 27].

Based on the initial materials, the vacancy clustering model or micro-explosion can be used to predict the formation of the nanostructures. In case of single crystalline or polycrystalline Ge, discrepancies to the uniform evolution of the nanopores as predicted by the vacancy clustering and micro-explosion theories have been observed. The study of the formation of nanopores by Darby et al. [19] have shown that the formation of nanopores happens in clusters. The void formation clearly showed a non-linear dependence on the dose.

Only a combination of the two theories can explain the formation of the porous structures in this case. Amorphization of the crystalline Ge leads to the formation of voids that are produced by micro-explosions. These voids then serve as nucleation points for vacancies to cluster. Thus the micro-explosion theory has been used to govern the nucleation of voids and vacancy clustering, which dictate the growth of voids. On the other hand, since amorphous Ge is assumed to possess inherent voids compared to crystalline Ge, formation of the nanopores can be explained just by using the vacancy clustering theory [21].

The occurrence of voids and their nucleation was not only restricted to vacancies that are already present in the material and the free surface, but also at solid-solid interfaces, as shown by Yates et al. [28].

1.6 Factors Affecting the Nanopore Formation

The number of point defects formed by irradiation is associated to the energy received by the target material atoms, which corresponds to the critical damage energy density, E_{dc} . The following relation gives the dose required for amorphization, D , at a depth z , from the surface, as determined by the critical damage energy density model:

$$D_z E_z = E_{dc} \quad (4),$$

where E_z is the damage energy at a depth z . Claverie et al. [29] calculated the value of E_{dc} at room temperature to be 5 ± 1 eV/atom.

The amorphization of Ge during ion beam irradiation is dependent on the irradiation temperature. The studies by Stritzker et al. [30] for a wide range of temperatures (-180 °C to 500 °C) showed that the occurrence of Ge amorphization could be classified into two distinct zones. The formation of amorphous layers was observed only when the temperature was below 200 °C. Since vacancies become extremely mobile above 200 °C, no amorphous layers were observed above 200 °C.

The out-of-plane volume expansion is only observed for the temperature range of 2 °C to 50 °C. The density of the nanoporous layer was approximately 30% of the bulk material. Mayr et al. [25] have shown that the process of amorphization produces strong compressive stresses, which can be relieved during the swelling process.

The out-of-plane displacement, h with respect to the original virgin surface at any point on the amorphous Ge layer is given by [20]:

$$h = h_m \left[1 - e^{(-a\phi+b)} \right] \quad (5),$$

$$a = \frac{n}{h_m \rho}$$

where h_M is the maximum displacement, n is the number of vacancies, ρ is the atomic density, a is a constant based on the number of vacancies and b is the fitting parameter.

The number of defects increases with the dose. Once the number of defects at a particular region reaches a critical value, they cluster together forming pores and settle into an amorphous state. The free energy of the region is reduced by this relaxation mechanism.

Annealing of amorphous Ge leads to recrystallization by the process of solid phase epitaxial regrowth. This recrystallization process follows the Arrhenius type law, where the rate of recrystallization, r is expressed as:

$$r = r_o \cdot e^{\left(\frac{-E_a}{kt}\right)} \quad (6),$$

where E_a is the activation energy, k is the Planck's constant and t is the associated temperature. Claverie et al. [29] have estimated r_o of Ge to be 3.05×10^{16} nm/s and E_a as 2.16 eV.

Using the law of conservation of mass, Romano et al. [31] have shown that the thickness of the nanostructured layer, h can be described by:

$$h = \frac{N}{\rho\pi DR^2} (\Phi - \Phi_o) \quad (7),$$

where N is the number of vacancies, ρ is the density of the element (Ge in this case), Φ is the ion dose, Φ_o is the nanostructuring threshold ion dose and R is the mean pore radius, which increases with the dose and decreases with temperature. A slight difference in the evolution pattern of the pores and the thickness of the porous layer was observed, based on the starting material (α -Ge or β -Ge) [19]. In single crystal and polycrystalline Ge, the porous structures produced were significantly longer and had a larger radius than the structures observed in amorphous Ge. The thickness of the nanostructured layer, produced by the irradiation of the crystalline Ge, was almost twice the thickness of the amorphous Ge layer.

1.7 Electrochemical Cycling of the Ge Anode

Although previous studies by Graetz et al. [13] showed that bulk Ge electrode exhibited good initial specific capacity, the electrode had a poor cycle life. The high strains caused by electrochemical cycling of the electrode seemed to be responsible for the complete loss of capacity after a few initial cycles.

The potential of ion beam modified Ge as an anode material for Li ion battery has been studied by Rudawski et al. [12, 32,]. The anodes were fabricated by depositing a thin film of Ge over 80 at% Ni and 20 at% Fe foil substrate using electron beam deposition. The Ni substrate acts as the current collector for the anode. Nanostructuring was rendered to a portion of this thin film anode by the process of ion beam modification, the details of which are described elsewhere [12]. The ion beam modification produced by the irradiation with Ge^+ resulted in an intermixing of about 5 nm, according to the SRIM-Monte carlo code, as shown in Figure 2.

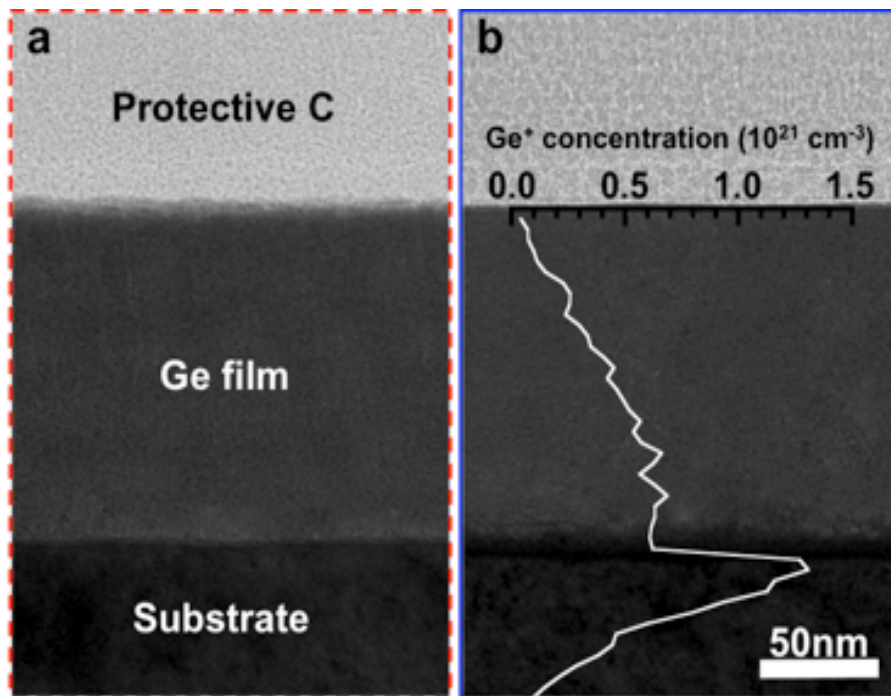


Figure 2. HR-XTEM images of a) the non-irradiated sample and b) the irradiated sample with superimposed Ge ion concentration profile. From [12], permission is in Appendix A.

The electrochemical behavior of as-deposited anode and nanostructured anode was studied against standard Li electrodes by galvanostatic testing (constant current), shown in Figure 3.

Since the Gibbs phase rule states that there is no change in voltage when more than one phase is present, the plateau region points out to the formation of different phases. The multiple peaks in the differential capacitance plot strongly suggest the existence of multiple Li-Ge phases.

During the initial cycles, the irreversible capacitance loss is due to the formation of the surface electrode interface. This loss may also be attributed to the absence of a natural oxide coating formation in Ge [12, 18, 32].

During the course of electrochemical cycling, the nanofeatures in the electrode tend to amass together. This process, known as electrochemical sintering, has been related to inherent instability of nanoparticles and the high surface to volume ratio. Electrochemical sintering and the stresses associated with electrochemical cycling cause two types of cracks, through-thickness cracks that convert the electrodes into isolated islands or patches and interface cracks that cause the loss of electrical conductivity between the electrode and the current collector.

The nanostructures anode material can and accommodate large stresses that develop during electrochemical cycling without intrafacial fracture of the anode. Although through-thickness cracks produce tiny isolated islands with a large elevation to width ratio, they remain attached to the current collector. In fact, the islands allow for relaxation of stresses associated with volume change and increased surface area due to the through-thickness cracks.

The electrochemical performance of the nanostructured electrodes was superior to that of the non-ion beam irradiated thin film electrodes. The as-deposited Ge electrode showed a rapid decrease in specific capacitance after a few cycles. The ion beam modified Ge electrode showed

no signs of capacitance fading, even after 25 cycles. Further, it also exhibited high discharge capacity and good Coulombic efficiency. Thus, it has been shown that the electrical contact between the current collector and the active anode material (Ge and Ni in this case) is a very important factor for the improved electrical performance of the battery. This primarily depends on the adhesion strength between the current collector and the anode.

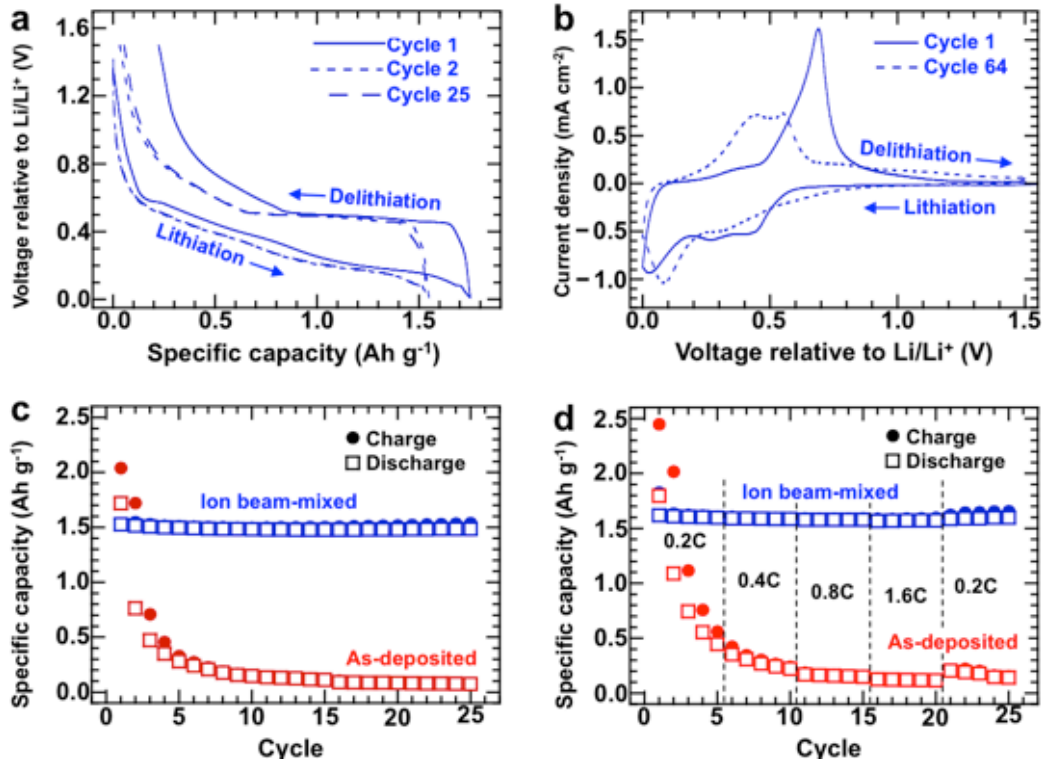


Figure 3. Electrochemical behavior of the Ge electrodes. a) various voltage curves for irradiated electrode b) cyclic voltammograms of the irradiated electrode different cycles c) cycle life plot of the irradiated and non-irradiated samples at a constant discharge rate of 0.4C d) cycle life plot of the irradiated and non-irradiated samples at various constant discharge rate. From [12], permission is in Appendix A.

In case of a thin film electrode, the large volumetric change that accompanies the coupling and decoupling of Li ions with the electrodes produces enormous mechanical stresses. These stresses cause two types of cracks, as shown in Figure 4, through-thickness cracks that

convert the electrodes into isolated islands or patches and interface cracks that cause the loss of electrical contact between the substrate current collector and the thin film electrode. The performance of the nanostructured electrodes suggests that the through-thickness crack did not deflect into the interface, thus rendering a good electrical and mechanical integrity between the current collector and the electrode. Thus, the performance of the battery is highly dependent on the adhesion of the thin film electrodes to the current collector [12]. The motivation for this research is to understand the role of ion beam irradiation in the improvement of adhesion strength of thin film Ge electrodes to the current collector, and to quantify the adhesion strength.

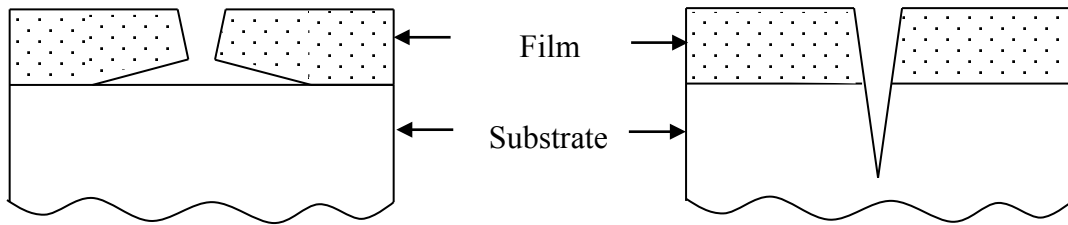


Figure 4. Schematics of a) interface crack and b) through-thickness crack.

CHAPTER 2

SELECTED RESULTS FROM FRACTURE AND CONTACT MECHANICS

2.1 Thin Film Adhesion

The ASTM defines adhesion as the phenomenon that causes two surfaces to be attached together by valence forces or mechanical clamping or by both together [33]. The thermodynamic work of adhesion can be described as the difference in surface energies between two different states, initially when two phases (e.g film and substrate) are in contact with each other in equilibrium, and when the two phases are separately in equilibrium with vapor (*in vacuo*) [34]. This is shown in Figure 5. In simple words, adhesion is defined as the energy required for breaking the forces of surface atoms, which are in contact at an interface.

Using the concept of energy conservation, the thermodynamic work of adhesion, W_T , can be represented as:

$$W_T = \gamma_f + \gamma_s - \gamma_{fs} \quad (8),$$

where γ_f , γ_s and γ_{fs} are the surface energies of the film, substrate and energy the interface respectively.

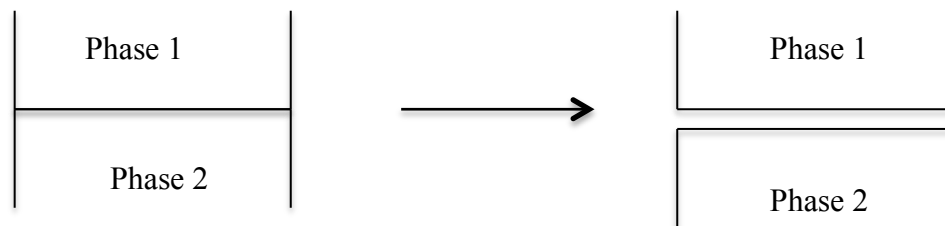


Figure 5. Two phases in equilibrium contact with each other and *in vacuo*.

2.1.1 The Surface Energy

The surface energy is greater than the energy associated with the bulk material. Surface energy can be defined as the sum of all the excess of all the energies of the atoms at the surface and it can be expressed in terms of the Gibbs (constant temperature and pressure) or the Helmholtz (constant temperature and volume) free energies. In terms of the Gibbs free energy, G , surface energy, γ can be expressed as:

$$\gamma = \left(\frac{dG}{dA} \right)_{T,P} \quad (9),$$

where A is the surface area.

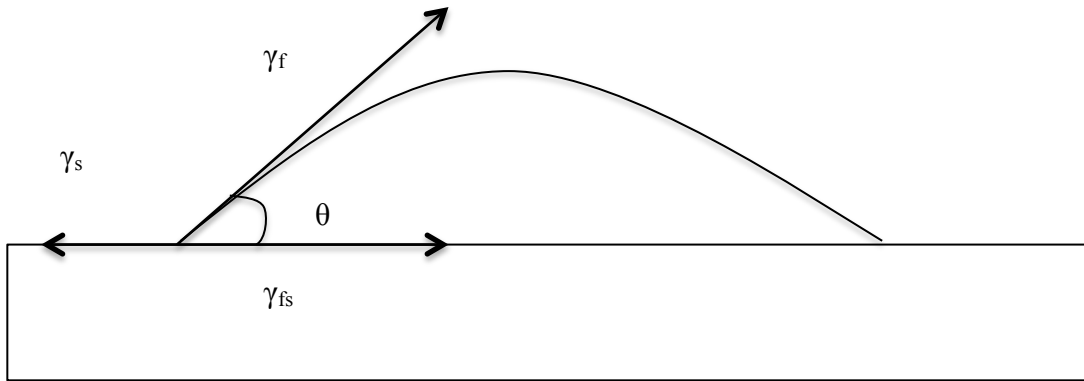


Figure 6. Surface energy and the contact angle.

2.1.2 The Contact Angle

The angle that the film makes with the substrate at the interface is termed as the contact angle, shown in Figure 6. Thomas Young first developed the concept of the contact angle back in 1805 [35]. For a liquid drop on a perfect solid the change in surface free energy, ΔG_s , accompanying a small change in the contact area, ΔA , can be expressed as:

$$\Delta G_s = \Delta A(\gamma_{sl} - \gamma_s) + \Delta A \gamma_l \cos(\theta - \Delta\theta) \quad (10).$$

At equilibrium, the change in free energy of the system with respect to the change in contact area is zero. This can be expressed as:

$$\lim_{\Delta A \rightarrow 0} \frac{\Delta G_s}{\Delta A} = 0$$

$$\gamma_{sl} - \gamma_s + \gamma_l \cos \theta = 0 \quad (11).$$

Young theoretically defines contact angle of a liquid drop on an ideal solid by the mechanical equilibrium of the liquid drop using the surface and interfacial energies. The Young's equation is expressed as:

$$\gamma_{sl} = \gamma_s - \gamma_l \cos \theta \quad (12).$$

Thus, from equation (12) it is clear that by knowing this contact angle, the interface energy can be easily calculated. Once surface energies of the bimaterial system and the interface energies are known, the work of adhesion can be obtained by substituting the values of interface energy in equation (8) and can be expressed as:

$$W_A = \gamma_f + \gamma_s - \gamma_{fs} = \gamma_f (1 + \cos \Theta) \quad (13).$$

This equation is known as the Young-Dupree equation.

2.1.3 Practical Work of Adhesion

In an ideal brittle material, the fracture energy is same as the thermodynamic work of adhesion, as the fracture takes place entirely by the breakage of atomic bonds of the surface atoms. However, scientific research is yet to show evidence of such ideal brittle material. Even in the case of the most brittle materials, there is a small amount of definite plastic energy dissipated during the fracture process.

In practical situations, the measured fracture energy, which is much higher than the thermodynamic work of adhesion W_T [34], is termed as the practical work of adhesion. The practical work of adhesion W_p can be expressed as:

$$W_p = W_T + C \quad (14).$$

The C term represents other energy dissipation terms. However, it is not an independent phenomenon and is a function of the thermodynamic work of adhesion. This can be better represented as:

$$W_p = W_T(1 + \varphi) \quad (15),$$

where φ depends on the working environment [34]. This relation shows that the modest increase in the thermodynamic work of adhesion results in a large increase in practical work of adhesion.

2.2 Fracture Mechanics Approach

According to the first law of thermodynamics, the change of the mechanical energy E_m of a system gets converted to the surface energy, E_s , internal energy, E_i , kinetic energy, E_k , and the dissipation energy, E_d . For a body with a crack length area A , the energy balance equation can be expressed as follows:

$$\frac{dE_m}{dA} = \frac{dE_s}{dA} + \frac{dE_i}{dA} + \frac{dE_k}{dA} + \frac{dE_d}{dA} \quad (16).$$

Since the internal energy is the stored elastic energy in the system, the equation can be rewritten as:

$$\frac{dE_m}{dA} - \frac{dE_i}{dA} = \frac{dE_s}{dA} + \frac{dE_k}{dA} + \frac{dE_d}{dA} \quad (17).$$

2.2.1 Griffith Energy Balance

When the kinetic energy, E_k , and the dissipation energy, E_d , energy are assumed to be negligible, the energy balance equation reduces to:

$$\frac{dE_m}{dA} - \frac{dE_i}{dA} = \frac{dE_s}{dA} \quad (18).$$

This relation is called the Griffith energy balance. The left part of the equation is related to the crack resistance force, R , and the right part of the equation is termed as the crack driving force, or the energy release rate, G .

The energy method of fracture mechanics, proposed by Griffith and developed to the present state by Irwin, dictates that a crack starts to grow once the crack driving force G is equal to or greater than the material's resistance to fracture, Γ . The source of material resistance to fracture may have various sources.

The potential energy of a body, E_p , is the difference between the elastic energy, U , and the work done by the external force, P . This can be expressed as:

$$E_p = U - P\delta \quad (19),$$

where δ is the displacement due to the external force.

Once the potential energy, E_p , is known, the crack driving force can be easily calculated. The energy release rate, G , is defined as the change in potential energy, E_p , with respect to the area of the crack A :

$$G = -\frac{dE_p}{dA} \quad (20)$$

At the initiation of crack growth, the strain energy release rate, G , is equal to the crack resistance force R ($G=R$). At this specific point of crack initiation, strain energy release rate reaches a critical value, ($G=G_c$), which is an indirect measure of the fracture toughness, Γ , of the

material. The energy release rate, G can be calculated by knowing the change in stiffness during the elongation of a crack. There are two methods in which the crack can be loaded. These are the fixed load and fixed grip conditions.

The fixed load method of loading the crack is also called the load control method. In this method a fixed load is applied to the cracked specimen. In this case, the work done by the external force is twice that of the strain energy of the system:

$$G_{C.P} = \frac{P}{2B} \left(\frac{d\delta}{da} \right) \quad (21).$$

Fixed grip method is also called the displacement control method. In this method, the displacement of the system is fixed and the work done by the external forces is zero ($dE_m=0$) and the strain energy of the system decreases. This can be represented by:

$$G_{C.G} = \frac{\delta}{2B} \left(\frac{dP}{da} \right) \quad (22).$$

In many practical situations, the compliance C , which is the inverse of the stiffness, has been used for estimating the G values.

$$G = \frac{P^2}{2B} \frac{dC}{da} \quad (23)$$

2.2.2 The Dundurs' Parameters

The solution for all interface crack problems depends on two non-dimension parameters, known as the Dundurs' parameters or elastic mismatch parameters [36]. When E , ν and μ are the Young's modulus, Poisson's ratio and the shear modulus of the film and the substrate, the Dundurs' parameters for plain strain conditions are given as follows:

$$\alpha = \frac{\bar{E}_f - \bar{E}_s}{\bar{E}_f + \bar{E}_s} \quad \beta = \frac{\mu(1-2\nu) - \mu_s(1-2\nu_s)}{\mu(1-\nu) + \mu_s(1-\nu_s)} \quad (24)$$

$$\bar{E} = \frac{E}{(1-\nu^2)} \quad \mu = \frac{E}{2(1+\nu)}$$

The Dundurs' parameters depend of the mismatch of the moduli between the materials. Thus, if the same material is used on either side of the interface, then there is no contribution by the Dundurs' parameters. The values of the two Dundurs' parameters flip when the materials at the interface are interchanged. The parameter α depends only on the Young's or tensile moduli of the materials and the parameter β depends on the bulk moduli of the materials. The values of the parameter α ranges from -1 to 1, depending on the stiffness or compliance of the top layer with respect to the bottom layer. There is no contribution by the Dundurs' parameter β , when extremely rigid materials are used in the system, due the absence of bulk moduli mismatch.

2.2.3 Stress Intensity Factor

The stress intensity factor, K , represents the singularity of the stress field around the crack tip before it approaches an infinite value. For an edge crack of length a , the stress intensity for three modes of the fracture are represented by [37]:

$$K_I = \sigma_{11} \sqrt{\pi a} \quad K_{II} = \sigma_{12} \sqrt{\pi a} \quad K_{III} = \sigma_{23} \sqrt{\pi a} \quad (25),$$

where σ in Figure 7 is the stress applied at a remote point from the crack tip. The subscript in K represents how the cracks are loaded, and I represent the presence of only normal stress, II represents pure in-plane shear and III represent twisting or out-of-plane shear stresses.

According to the stress intensity approach, the failure of materials caused by crack growth occurs when the stress intensity factor, K , exceeds the critical stress intensity factor, K_{IC} ($K \geq K_{IC}$). The critical stress intensity factor is a measure of the toughness of the material.

The cracks problems in isotropic materials, are predominantly mode I in nature. However, interface crack problems are mostly multi-mode in nature. This is due to the difference

in elastic properties of the materials and asymmetric loading conditions that exist at the interface. The stress intensity factor for the interface problems comprising of the two isotropic materials can be expressed in the complex form as:

$$K = K_I + iK_{II} \quad (26),$$

where K_I governs the normal tensile forces and the related normal separations, while K_{II} represents the planar shear forces and the related displacements at the interface crack.

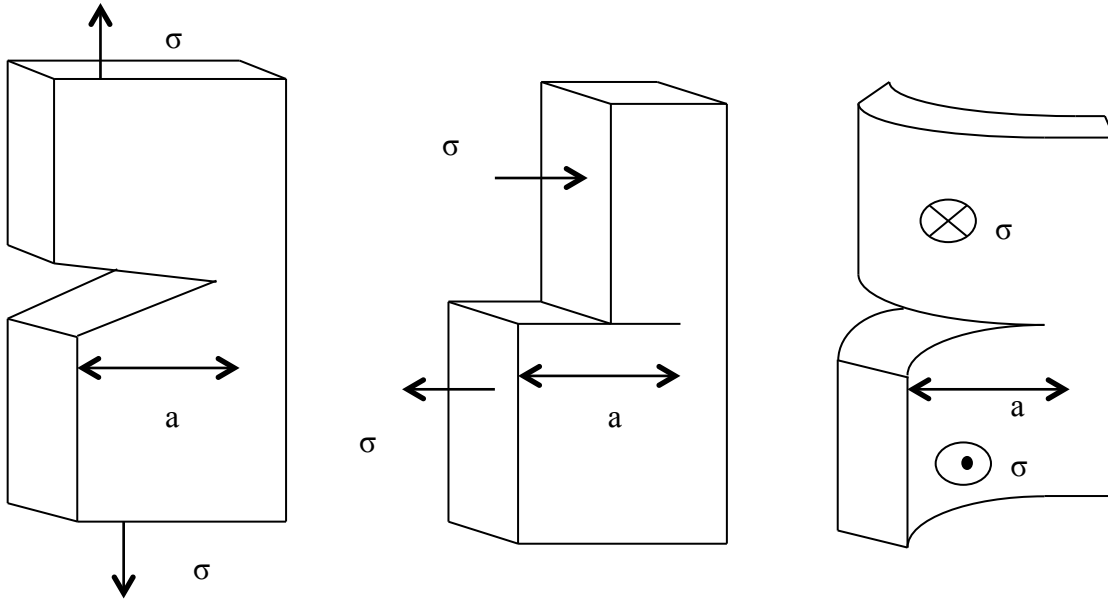


Figure 7. Modes of fracture.

The complex stress intensity factor can also be expressed in terms of the load, P , that produces a bending moment, M , on the bimaterial system as [38]:

$$K = \left(\frac{P}{c_1 h^{1/2}} - i e^{i\gamma} \frac{M}{c_2 h^{3/2}} \right) \frac{p}{2^{1/2}} e^{i\omega} h^{-i\epsilon} \quad (27),$$

where h is the thickness of the film, γ is an angle, which depends on the system, ω is the real angular function, p and ϵ are bimaterial constants, which depend on the Dundurs' parameters.

The singularity of the shear and normal stresses at a distance r from the crack tip can be expressed using the complex stress intensity factor as:

$$\sigma + i\sigma = \frac{(K_I + iK_{II})r^{i\varepsilon}}{\sqrt{2\pi r}} \quad \varepsilon = \frac{1}{2\pi} \ln \left(\frac{1-\beta}{1+\beta} \right) \quad (28),$$

where ε depends on the Dundurs' parameter, as shown above.

The crack tip opening displacement at a distance r from the crack tip can be expressed as:

$$\delta + i\delta = \frac{4}{\sqrt{2\pi}} \frac{\left(\frac{(1-\nu_1^2)}{E1} + \frac{1-\nu_2^2}{E2} \right)}{(1+2i\varepsilon) \cosh(\pi\varepsilon)} (KI + KII) r^{\frac{1}{2}+i\varepsilon} \quad (29).$$

Using the stress intensity approach, the energy release rate for the combined modes I, II and III is given by:

$$G = \frac{K_I^2 (1-\nu)}{E} + \frac{K_{II}^2 (1-\nu)}{E} + \frac{K_{III}^2}{2\mu} \quad (30).$$

In case of a thin film deposited on top a thick substrate, the debonding of the thin film caused by the crack is driven by the intrinsic biaxial stress in the film, σ . Once the interference crack length is much greater than the thickness of the film, h , the energy release rate reaches a steady state, which becomes independent of the crack length, a , and can be expressed as:

$$G = \frac{1}{2} \frac{(1-\nu_f^2)\sigma^2 h}{E_f} \quad (31).$$

2.2.4 The Phase Angle

Due to the mixed mode nature of fracture at interfaces, the ratio of the shear to the tensile components involved is expressed using the phase angle, Ψ . For an ideally stiff bimaterial

interface, where $\beta=0$, the phase angle in terms of ratio of the stress intensity factors can be expressed as:

$$\Psi = \tan^{-1}\left(\frac{K_{II}}{K_I}\right) \quad (32),$$

and in terms of the remote in-plane shear and the normal stresses, Ψ , can be expressed as:

$$\Psi = \tan^{-1}\left(\frac{\sigma_{12}}{\sigma_{22}}\right) \quad (33).$$

Thus, Ψ gives a measure of the phase of the stress intensity factors. It can be observed that when $\Psi = 0$, only uniaxial tensile opening exists (mode I). Similarly, $\Psi = 90^\circ$ signifies that the loading is completely in-plane shear in nature (mode II) [39]. This is shown in Figure 8.

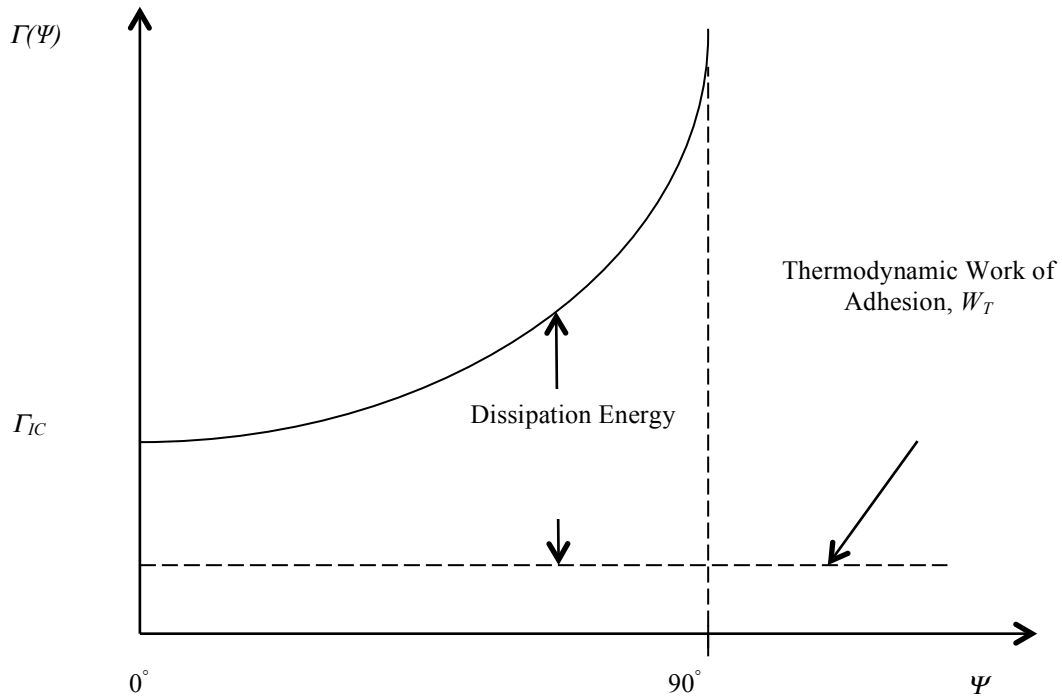


Figure 8. Interface energy as a function of phase angle. Adapted from [70].

The phase angle for a bimaterial system under a bending moment M due to the load P can be expressed as follows:

$$\Psi = \tan^{-1} \left[\frac{\iota \sin \omega - \cos(\omega + \gamma)}{\iota \cos \omega + \sin(\omega + \gamma)} \right] \quad (34).$$

$$\iota = \frac{c_1 Ph}{c_2 M}$$

where h is the film thickness c_1 and c_2 are bimaterial constants, γ is a bimaterial system dependent angle and ω is the real angular function.

In case of a thin film bimaterial system, where the thickness of the substrate is much greater than the film thickness, the plain strain stress intensity factor [39] is given by:

$$KI = \frac{P}{(2h)^{1/2}} \cos(\omega) + \frac{\sqrt{6M}}{h^{3/2}} \sin(\omega) \quad (35)$$

$$KII = \frac{P}{(2h)^{1/2}} \sin(\omega) - \frac{\sqrt{6M}}{h^{3/2}} \cos(\omega) \quad (36)$$

For a bimaterial system, the strain energy release rate at the interface is dependent on the Dundurs' parameter and can be expressed as:

$$G = \frac{(1-\beta^2)}{2} \left[\frac{1-\nu_1^2}{E_1} + \frac{1-\nu_2^2}{E_2} \right] (K_I^2 + K_{II}^2) \quad (37)$$

The energy release rate of the interface depends on the roughness of the interface where the fracture happens. This roughness factor depends on the material properties, like the Young's modulus, intrinsic toughness and also the geometric parameters of the facets in contact at the interface.

At a bimaterial interface, where the crack loading is of mixed mode type, the growth of the crack starts when the energy release rate, G , is equal to the interface toughness, Γ , which is a function of the phase angle, Ψ . The dependence of the strain energy release rate on the mode mixity is given by the following equations:

$$G(\Psi) = \Gamma_i^c [1 + (1 - \lambda) \tan^2 \Psi] \quad (38),$$

$$G(\Psi) = \Gamma_i^c \left\{ 1 + \tan^2 [\Psi(1 - \lambda)] \right\} \quad (39),$$

where Γ_i^c is the pure mode I fracture toughness and λ is an adjustable parameter, which depends on the influence of mode II on the interfacial toughness.

Generally, the fracture toughness, Γ , of the material varies proportional to the phase angle, Ψ . This suggests that the delamination of the thin film is more likely to happen due to predominantly tensile component, and is less likely to happen in the case, where a predominant shear component is associated with the film/substrate system.

2.3 Contact Mechanics

Contact mechanics is the study of the distribution of stresses and the displacements involved when bodies are in contact. The nanoindentation technique is an extension of the indentation theory, based on contact mechanics. The concept of indentation originated from the work of Hertz, who first started analyzing the contact of isotropic elastic bodies.

When two bodies are forced against each other, the body made of the harder material scratches or indents the other body. This was the principle behind the Mohr's scale, which ranked materials based on their relative hardness. In the Mohr's scale, diamond, the hardest naturally occurring substance was assigned the top value of 10 and other materials were given a lesser number, based on the relative hardness [47].

Hertz [68 - 69] initially analyzed the contact of elastic bodies. When a rigid sphere comes in contact with a rigid sphere, Hertz was able to relate the radius of the rigid sphere, R , the applied load, P , and the reduced modulus to the contact circle of radius, a as:

$$a^3 = \frac{3PR}{4E_r} \quad (40).$$

When a sample of interest is indented using a rigid indenter, the reduced modulus, E_r , can be expressed as:

$$\frac{1}{E_r} = \frac{1-\nu^2}{E} + \frac{1-\nu_l^2}{E_l} \quad (41),$$

where E , E_l , ν , and ν_l are the Young's modulus and Poisson's ratio of the sample and the indenter respectively.

The distribution of stress and deformations in elastic bodies when they come in contact with a rigid indenter was first studied by Boussinesq et al. [42], using the potential energy approach. Sneddon solved the Boussinesq problem using the Henkel transformation and was able to relate the applied load and the depth of indentation for a flat-ended cylindrical punch. He later extended this relation between applied load and depth of indentation to an axisymmetric arbitrary profile. During the indentation of a material of bulk modulus of μ , and Poisson's ratio of ν , for a conical indenter with a semi cone angle, α , the applied load, P , can be related to the depth of indentation, h , by the relation:

$$P = \frac{4\mu \cot \alpha}{\pi(1-\nu)} h^2 \quad (42),$$

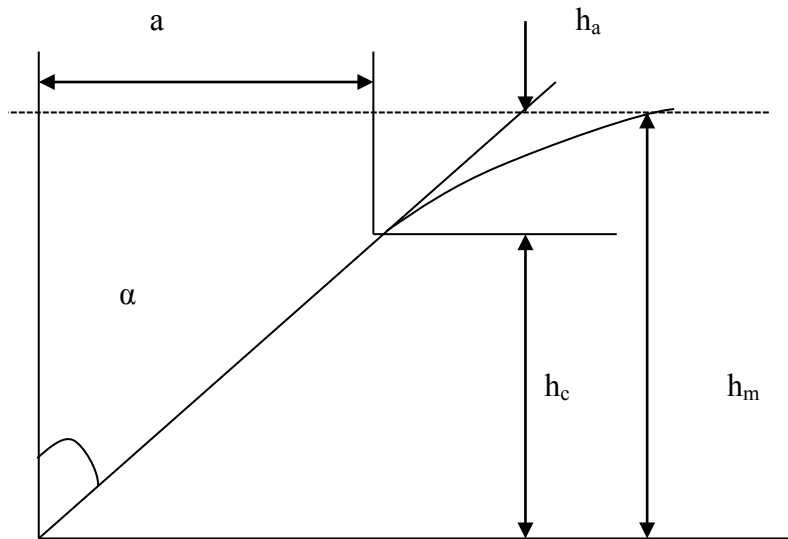


Figure 9. Indentation schematic of a conical indenter. Adapted from [47].

From the indentation schematics for a conical indenter in Figure 9, it can be observed that the total depth of indent h_m comprises of two parts. The first part is the contact depth h_c , which is the distance from the point of contact of the indenter to the bottom of the indenter. The next part, h_a , is the depth from the surface to the point of contact.

The technique is very similar to normal indentation and the micro-indentation tests. The striking difference between nanoindentation and traditional indentation method is the use of depth sensing mechanism, which is used to calculate the area of the imprint. The imprint area can be calculated knowing the geometry of the indenter and the depth of the indent.

2.4 Load-Displacement Curves

The primary aim of the nanoindentation test is extracting the load and the displacement values during indentation, from which two important mechanical properties; namely, Young's modulus and hardness can be calculated.

The load-displacement diagram has two main regions: the loading portion and the unloading portion. In the loading curve, there exists a state of purely elastic loading, up to a

certain point after which the loading becomes elastic-plastic in nature. In case of ductile materials, the point of transition from pure elastic loading to elastic-plastic loading is called the yield point. The initial portion of the unloading curve is also elastic in nature, after which it becomes elastic-plastic unloading. h_m represents the maximum depth of indentation, h_e is the recovered elastic depth and h_f is the depth of permanent residual impression due to plastic deformation. A sample load-displacement curve is shown in Figure 10.

Experiments have shown that load and depth have a quadratic relation during loading. The slope of the elastic part of the unloading curve is known as contact stiffness, ($S = dP/dh$). The contact stiffness is related to the reduced Young's modulus, E_r , and the contact area, A [43] as:

$$S = \frac{2}{\sqrt{\pi}} E_r \sqrt{A} \quad (43).$$

The projected contact area, A , can be calculated knowing the contact depth, h_c , and the geometry of the indenter. To estimate the contact depth, h_c , it is necessary to curve-fit the unloading portion of the curve. Initially, a linear fit from the upper one-third portion of the unloading curve was suggested. However, some materials exhibited a highly curved unloading curve. A second order polynomial fit was introduced to account for this curve. Later, Oliver and Pharr [44] suggested a simple power fit for the unloading curve. This power law can be expressed as:

$$P = A(h_m - h_f)^m \quad (44),$$

where $h_m - h_f$ is the recovered elastic depth while A and m are adjustable fitting parameters.

The mean contact pressure, p_m , is defined as the ratio of the applied load, P , during the indentation process to the contact projected area, A . This can be represented as: $p_m = P/A$.

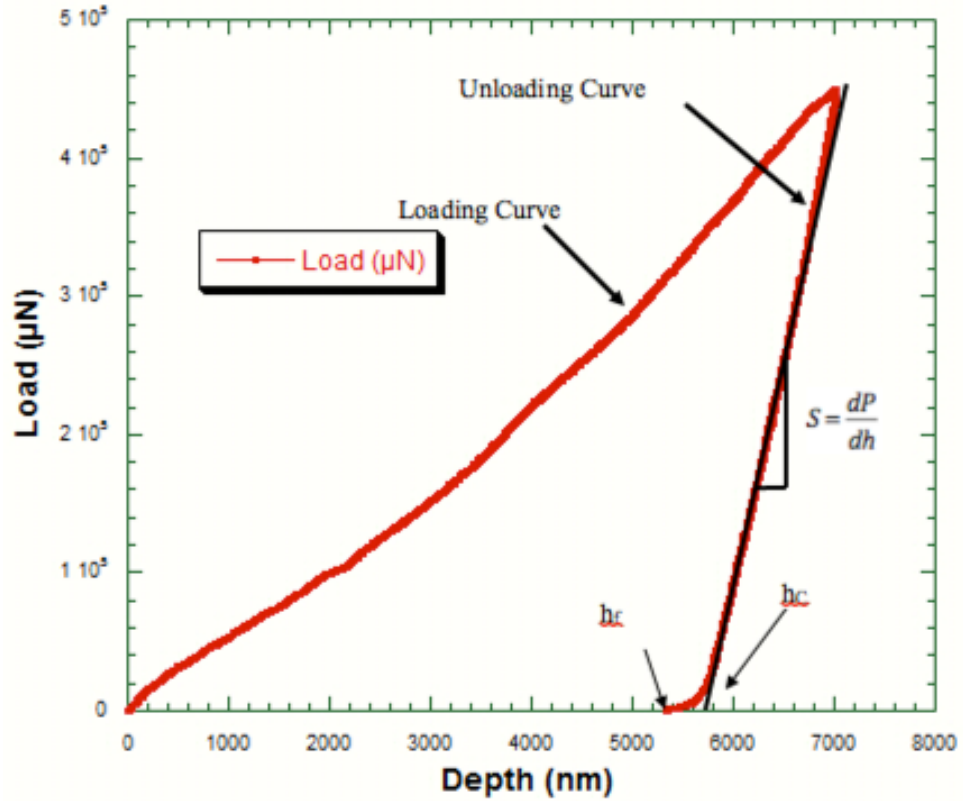


Figure 10. A sample load-displacement curve.

It has been shown that beyond a threshold point, the mean contact pressure, p_m , becomes independent of the applied load. Above the threshold point, the materials have shown to exhibit a complete plastic response and the mean contact pressure, p_m , is proportional to the hardness, H , of the material. The hardness values can be expressed as:

$$H = \frac{P}{A} \quad (45),$$

where P is the applied load and A is the projected area. The hardness can be related to the yield stress of the materials relation as:

$$H \approx KY \quad (46),$$

where Y is the yield strength and K is the constrain factor, which depends on the type of indenter/specimen and other experimental parameters [45]. For materials with a large E/Y ratio, the value of K is around 3. At many practical situations, the hardness values are calculated before the response of the material is entirely plastic. At such conditions, the mean contact pressure is not independent of the applied load and this may lead to errors in hardness values.

2.5 Expanding Cavity Model

There are various semi-empirical models, which predict the experimental results of nanoindentation. One such model is the expanding cavity model. In this model, during the process of indentation, a hydrostatic core of radius a_c encloses the surface of the indenter. A hemispherical plastic zone of radius c in turn encloses the hydrostatic core. An increment of the indentation depth also results in the expansion of the core by da , which is accommodated by a radial movement at the core boundary. This in turn increases the plastic zone by an amount dc . For geometrically similar indenters, like the conical indenter, for a semi cone angle of a , it can be shown that the rate of increase in plastic zone and the core are the same ($da/dc = a/c$). The schematic of this model is shown in Figure 11.

Johnson [46] showed that the pressure in the core, p , can be calculated using the relation:

$$\frac{p}{Y} = \frac{2}{3} \left\{ 1 + \ln \left[\frac{\left(\frac{E}{Y}\right) \tan \beta + 4(1-2\nu)}{6(1-\nu)} \right] \right\} \quad (47),$$

where p is the pressure and β is the angle of inclination of the indenter with the surface of the specimen. The mean contact pressure is related to the pressure inside spherical region, p , and the yield strength of the material, Y , as:

$$p_m = p + \frac{2}{3}Y \quad (48),$$

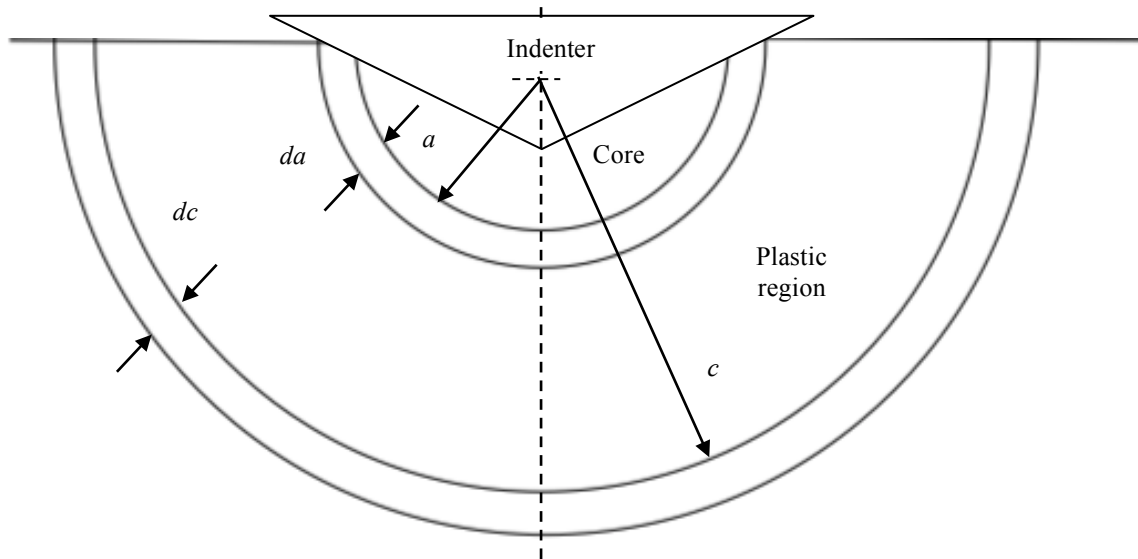


Figure 11. Schematic of the expanding core model. Adapted from [47].

2.6 Pile-up and Sink-in

When an indenter indents a material, the surface around the indenter tip is not flat and the surface tends to get displaced in an out-of plane fashion. When the material around the indenter sinks below the surface level, the out-of plane displacements are termed as ‘sink-in’ and when the material around the indenter rises above the surface level, the out-of-plane displacements are termed as pile-up. These phenomena are important, as pile-up increases the contact area and the sink-in reduces the contact area of the indenter with the surface. For polycrystalline materials, the strain-hardening nature of the materials has been used to account for these out-of-plane displacements [42]. When an annealed material that has very little internal strains is indented (high strain energy potential), the materials around the indenter tends to sink-in. On the other hand, when a highly pre-strained material (material with low strain energy potential) is indented, the material around the indenter tends to pile-up. However, this is not the case when the single crystal materials are indented, as the pile-up or sink-in phenomena depend on the strain-hardening rate of the material. Most single crystal materials exhibit a distinct pile-up when

indented. A very small quantity of pile-up has also been observed during the indentation of brittle material [44 - 45].

Some of the most commonly used methods for interfacial toughness measurement are discussed in the following chapter.

CHAPTER 3:

THEORIES OF ADHESION MEASUREMENT AND RESIDUAL STRESSES

3.1 Thin Film Adhesion Measurement Techniques

3.1.1 Four-point Bending

The four point bending method uses the concept of beam theory to calculate the strain energy release rate. Charalambides et al. [48] developed an equation for the energy release rate, G_{ss} , which can be expressed as:

$$G_{ss} = \frac{P^2 l^2 (1 - \nu_f^2)}{8 d^2 E_f} \left(\frac{1}{I_s} - \frac{\lambda}{I_c} \right) \quad (49),$$

$$\lambda = E_s (1 - \nu_f^2) / E_f (1 - \nu_s^2) \quad I_s = \frac{h_s^3}{12} \quad I_c = \frac{h_f^3 + \lambda h_s^3}{12} + \frac{\lambda h_f h_s (h_f + h_s)^2}{4(h_f + \lambda h_s)}$$

where I_c is the area moment of inertial of the composite beam, M is the moment per unit width, and P is the total load and l is the distance between the inner and outer load lines.

The energy release rate can be calculated as the difference in strain energies between the cracked and non-cracked beams. Thus, knowing the geometry, Young's moduli and the Poisson's ratios (material properties) of the specimen, the G_{ss} value can be calculated by measuring the load P at which steady state crack growth happens. However, equation (49) is valid only for a special case of a symmetric crack.

From equation (49), it can be inferred that the ratio of the moduli of the materials has a high impact on the strain energy release rate. The test specimen consists of a thin film over a

substrate and a notch, which is made along the entire width of the sample. The application of controlled loads on the test specimen, clamped on two sides, produces a symmetric pre-crack of the length $2a$ at the interface. The schematic of this test specimen is shown in Figure 12.

When metallic substrates are used, the geometry of the test specimen should be selected in a manner such that the interface failure occurs before the plastic deformation of the substrate. Such situations exist when the substrate thickness is greater than the film thickness [49].

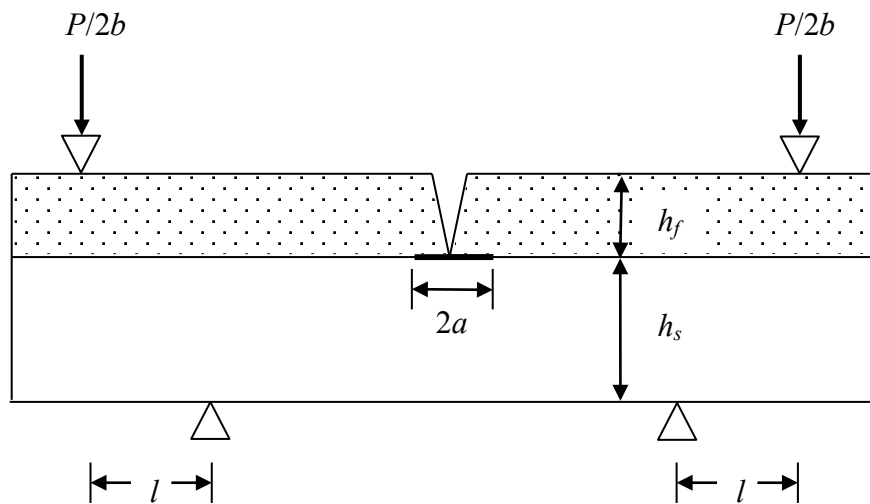


Figure 12. Schematic of a four-point bend test specimen. Adapted from [48].

Four point bending is one of the most popular methods of measuring thin film adhesion in the semiconductor industry [50 - 51]. However, it has been observed that that pre-cracks are generally not symmetric and there is only growth of one side of the crack. The numerical solution for the strain energy release rate for such conditions is given elsewhere [52].

3.1.2 The Superlayer Test

Early thin film adhesion tests had the inadequacy to quantitatively measure interfacial toughness. This motivated Bagchi et al. [53] to develop the superlayer test. The energy release rate for a crack in a bimaterial system can be expressed as:

$$G = \Xi \frac{(1 - \nu_f) \sigma^2 h_f}{E_f} \quad (50),$$

where E_f , ν_f represents the Young's modulus and the Poisson's ratio of the film, h_f is the film thickness, σ is the stress in the film. Ξ is a crack type and elastic mismatch dependent. The values for Ξ are given else where [38]. For a wide film with biaxial stress, σ_f , the steady state strain energy release, G_{ss} , can be expressed as:

$$G_{ss} = \frac{(1 - \nu_f)}{E_f} \sigma_f^2 h_f \quad (51),$$

where h_f , E_f and ν_f are the thickness, the Young's modulus and Poisson's ratio of the film.

In a typical thin film with a biaxial residual stress, the strain energy release rate values are much lower than the practical debond energies of the system. Thus, to give a good measure of the adhesion energy of the system, the G_{ss} value must be increased without affecting the phase angle of the system. Since G_{ss} is directly proportional to the film thickness, a method of increasing the value of G_{ss} is by the application of a thick superlayer over the thin film. The increases the G values due to the superlayer deposition does not the phase angle, Ψ , provided they meet the following conditions [54]:

- 1) The superlayer is deposited over the thin film at room temperature;
- 2) The superlayer must process a large compressive stress on deposition;
- 3) The superlayer must not react with the thin film.

The experimental specimen as shown in Figure 13 has a pre-crack in the form of a graphite layer between the substrate and the thin film. The half width of the graphite layer, which acts as the pre-crack, is approximately twice the thickness of the film. The under-layer is thermally evaporated over the substrate and patterned using photolithography techniques. This

process ensures the formation of release layers that is free of edge defects [55]. The thin film is deposited over the graphite release layer, which is followed by the deposition of the superlayer over the film.

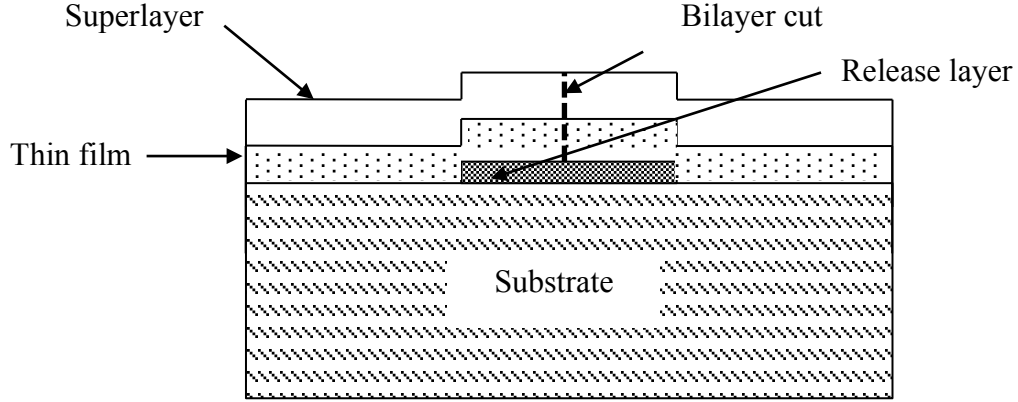


Figure 13. Schematic of a superlayer test. Adapted from [53].

Finally, a cut is made in the bilayer, just above the release layer. The bilayer remains attached to the substrate when the strain energy release rate is less than the debond energy of the system ($G_{ss} < \Gamma$), or debonds when the strain energy release rate is greater than the debond energy of the system ($G_{ss} > \Gamma$). It is observed that the debonding occurs at a critical thickness of the superlayer. Thus, when no debonding is observed, a thicker superlayer should be used for evaluating G_{ss} . The energy release rate for the superlayer [55] can be expressed as:

$$G = \sum_i \frac{\sigma_i^2 h_i}{E_i} - \sum_i \frac{1}{E_i} \left[\frac{P^2}{h_i} + \frac{12M_i^2}{h_i^3} \right] \quad (52),$$

$$P = k \left[\frac{E_1' h_1^3 + E_2' h_2^3}{6(h_1 + h_2)} \right] \quad k = \frac{6(h_1 + h_2)(\epsilon_1 - \epsilon_2)}{h_1^2 + \frac{E_2' h_2^3}{E_1' h_1} + \frac{E_1' h_1^3}{E_2' h_2} + h_2^2 + 3(h_1 + h_2)^2}$$

$$M_i = E_i' k \quad E_i' = \frac{E_i}{(1-\nu_i)}$$

where $i=1, 2$ represents the thin film and the superlayer, h_i , E_i are the thickness and Young's moduli of the respective layer and k is the radius of curvature of the bilayer. Although the superlayer technique provides accurate strain energy release rate values, the measurement of adhesion values is restricted to a phase angle of 50° [54].

3.1.3 One-dimensional Buckling

For a thin isotropic film, in a state of biaxial stress, over a thick substrate, the one dimensional buckling analysis was provided by Hutchinson and Suo [38]. When the thickness of the thin film is very small, compared with the radius of the blister, the film buckling can be modeled analogous to the buckling of a column. In such a case, the Euler's critical buckling stress is given by:

$$\sigma_{CB} = \frac{\pi^2}{12} \frac{E_f}{(1-\nu_f)} \left(\frac{h_f}{a} \right)^2 \quad (53),$$

where h_f is the thickness of the film, a is the radius of the blister, E_f and ν_f are the Young's modulus and Poisson's ratio of the film. From equation (53), an inverse relation between the critical buckling stress and the blister radius is observed.

When the residual compressive stress in the film is equal to or greater than the critical buckling stress ($\sigma_R \geq \sigma_{CB}$). This process of buckling, relieves the stresses in the film and the strain energy release rate, G , can be expressed as:

$$G = \left[\frac{(1-\nu_f^2)h_f}{2E_f} \right] (\sigma_R + 3\sigma_{CB})(\sigma_R - \sigma_{CB}) \quad (54).$$

3.1.4 Nanoindentation Test for Fracture

Strength and resistance to fracture are the two primary components that constitute the adhesion properties of materials. The Marshall and Evans's analysis focuses particularly on the quantitative measurement of the fracture resistance component of adhesion by using a nanoindentation technique to produce a controlled interface crack.

Marshall and Evans [56] calculated the energy release rate of an indented film with residual compressive stress using a hypothetical four-step process shown in Figure 14. In the first step, the portion of the film above the interface crack length is cut and taken out. Stresses of equal magnitude, but of tensile nature, are applied to the edges of the uncut portion and the film. The cut portion of the film is relieved of the compressive stresses and this produces an expansion, which is given by:

$$\Delta R = \frac{(1-\nu_f)\sigma_R a}{E_f} \quad (55),$$

where E_f , ν_f are the Young's modulus and Poisson's ratio of the film, σ_R is the residual stress in the film and a is the length of the crack. The work done can then be expressed as:

$$U_p = \frac{\pi h(1-\nu_f)\sigma_R^2 a^2}{E_f} \quad (56).$$

Since the total energy of the system for an unbuckled plate is independent of the crack length, the strain energy in the remainder of the film, $U_S = U_R - U_p$, must be dependent on the crack length.

In the second step, when the film is indented, a plastic zone is created around the indenter. According to the conservation of mass, the indentation volume, V_I , in the internally pressurized plastic zone produces a radial expansion that can be expressed as:

$$\Delta_I = \frac{V_I}{2\pi ah} \quad (57),$$

and the work done due this volume expansion Δ_I is given by:

$$U_I = \frac{\pi h(1-\nu_f)^2(C_0 - \sigma_I^2 a^2)}{2E_f} \quad (58),$$

where C_0 is a crack length-independent constant.

In the third step, the residual and the indentation stresses are reapplied to the film and the work done by the application of the combined stresses can be given by:

$$U_T = \frac{\pi h(1-\nu_f)a^2}{E_f} \left[(\sigma_R + \sigma_I)^2 - (1-\alpha)(\sigma_R + \sigma_I - \sigma_{BC})^2 \right] \quad (59),$$

where α is the slope of the buckled portion in the buckling load versus edge displacement diagram, and can be expressed as:

$$\alpha = 1 - \frac{1}{1 + 0.902(1-\nu_f)} \quad (60),$$

and in case of an unbuckled film, the value of α is one.

In this model, if the circular delaminated film were to buckle, the perimeter of the delaminated region experiences a tensile stress and the release of stored strain energy leads to the development of the cracks.

In the final step, the film is compressed and inserted back into the initial cavity, and the strain energy release rate is estimated by differentiating the sum of all these strain energies with respect to the area of the crack, A . This can be expressed as:

$$G = \frac{h(1-\nu_f)}{E} \left\{ \sigma_R^2(1-\alpha) + \sigma_I^2 \left[\frac{(1+\nu_f)}{2} - (1-\alpha) \left(1 - \frac{\sigma_{BC}}{\sigma_I} \right)^2 \right] \right\} \quad (61).$$

From the equation (61), it is clear that in case of non-buckling fracture strain, energy release rate term depends solely on the stress supplied by the indentation process. Although the Marshall and Evan's model produced accurate strain energy release rate values for a wide range of phase angles, it did not work well in case of ductile films on a brittle substrate. This is due to the plastic deformation, which occurs in the case of ductile films before delamination. Another problem associated with the indentation technique is pile-up and sink-in, which may occur around the indenter tip.

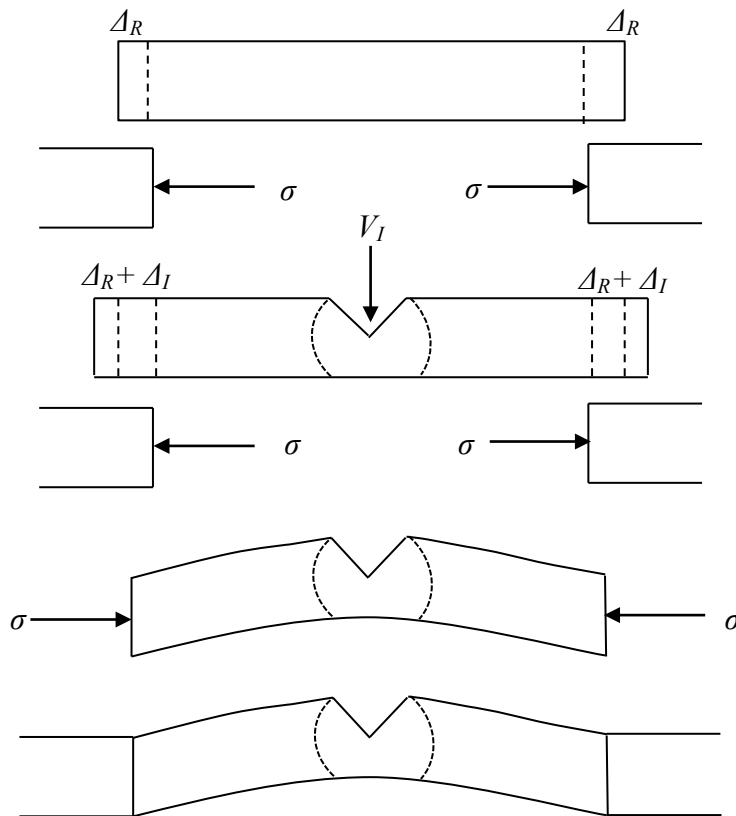


Figure 14. Hypothetical steps used for strain energy calculation. Adapted from [56].

3.1.5 The Superlayer Indentation Test

Kriese and Gerberich [57] developed the superlayer indentation test method. This method successfully overcomes the limitations of the previous tests for interface adhesion measurement

by combining the concepts of both, the superlayer and the indentation tests. In this technique a highly stressed and thick superlayer is deposited over the film of interest as shown in in Figure 15 and the strain energy release rate of bilayer is calculated using composite laminate theory.

The strain energy release rate values of the bilayer have been shown to approach the values of the single layer on two separate occasions:

- 1) Thickness of the superlayer is much greater compared to the film thickness;
- 2) Thickness of the superlayer approaches zero.

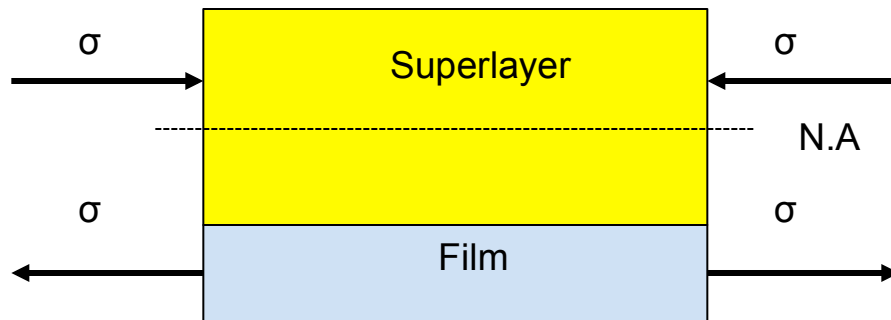


Figure 15. Stresses in a superlayer indentation test specimen. Adapted from [57].

The deposition of a highly compressed superlayer provides extra driving force for delamination. The superlayer indentation test has various advantages. The energy release rate value of the problematic ductile films over brittle substrate can be easily calculated using this technique. Thin films can also be tested in the as-processed state as a tailor-made superlayer for that specific condition can be deposited over the coating. The deposition of a highly stressed superlayer also eliminates the need for multiple superlayers.

3.1.6 Microwedge Indentation Test

Vlassak et al. [58] developed a method to measure the adhesion of brittle films bonded to ductile substrates. The striking difference of this method from the previously used adhesion testing methods is the use of a wedge indenter that loads the crack in a plane-strain fashion.

During the adhesion tests using axisymmetric indenters, there is a possibility of the formation of radial cracks in the thin film as the result of the tensile hoop stresses that develop during the indentation process. The development of these radial cracks, hinder the extraction of accurate adhesion values. These problematic tensile hoop stresses could be avoided by the use of a plane-strain wedge indenter. In case of the wedge indenter, instead of the hoop stress, a compressive stress that acts parallel to the indenter is produced. The strain energy release rate based on this plane-strain model is given by:

$$G = \frac{(1-\nu_f^2)h\sigma_{xx}^2}{2E_f} \quad (62),$$

where σ_{xx} is the stress perpendicular to the indenter. It has been shown that for a film with a residual stress σ_R , the σ_{xx} due to indentation can be expressed as:

$$\sigma_{xx} = \sigma_R - \left(\frac{E_f}{1-\nu_f} \right) \frac{w^2 \tan \beta}{\pi a^2} \quad (63),$$

where w is the half width of indentation, a is the crack length and β is the angle made by the face of the indenter to the surface of the sample.

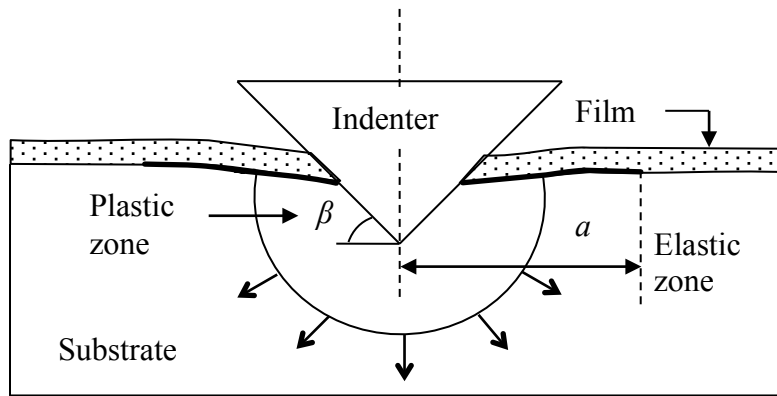


Figure 16. Schematic of the micro-wedge indentation test. Adapted from [58].

3.1.7 The Drory and Hutchinson Model

In the case of a brittle film over a ductile substrate, where a large load needs to be applied to delaminate the coating from the substrate, Drory and Hutchinson [59] provided the expression for the strain energy release rates. During the process of indentation, the Boussineq's solution [60] for the radial displacement is valid only for points far from the indenter tip. It was shown the radial displacements, u , can be expressed as:

$$\ln\left(\frac{u}{a}\right) = b_0 + b_1\left(\frac{r}{a}\right) + b_2\left(\frac{r}{a}\right)^2 + b_3\left(\frac{r}{a}\right)^3 \quad (64)$$

where r is the delamination radius, a is the radius of indentation and b_0, b_1, b_2, b_3 are the constants which depend on the coating/substrate pair, given else where [59].

This model relies primarily on the total radial strains, ε_{Tr} , and tangential strains, $\varepsilon_{T\theta}$, which develop as a result of the residual stresses and indentation. The strains due to indentation can be expressed as:

$$\varepsilon_r = \frac{du}{dr} \quad \varepsilon_\theta = \frac{u}{r} \quad (65),$$

and the strains due to the residual stress, ε_0 , can be expressed as:

$$\varepsilon_0 = \frac{(1-\nu)\sigma_0}{E} \quad (66),$$

The total strains, which is the sum of the strains produced by the indentation and the residual stresses can then be expressed as:

$$\varepsilon_{Tr} = \varepsilon_r + \varepsilon_0 \quad \varepsilon_{T\theta} = \varepsilon_\theta + \varepsilon_0 \quad (67).$$

The in-plane strain energy per unit area, U , of the coating is another important parameter that can be deduced by knowing the total strains in the radial and tangential directions. This can be expressed as:

$$U = \frac{1}{2} \frac{E_f h}{(1 - \nu_f^2)} (\epsilon_{Tr}^2 + \epsilon_{T\theta}^2 + 2\nu \epsilon_{Tr} \epsilon_{T\theta}) \quad (68)$$

It is clearly seen from the above equation that the strain energy per unit area is highly dependent on the ratio of displacement in the radial direction, r , to the radius of indentation, a . At points where the radial displacement is much greater than the radius of the indenter, strain energy per unit area reaches a steady state value, which can be expressed as:

$$U_0 = \frac{1}{2} \frac{E_f h}{(1 - \nu_f^2)} (\epsilon_0^2) \quad (69).$$

Once the total tangential and radial strains are known, the process of delamination can be analyzed and the strain energy release rate values can be calculated by using either one of the three models that have been described by Drory and Hutchinson, depending on the nature of delamination. The three models are as follows:

- 1) Delamination with the break-up of the detached film with only a very small strip of film left behind the advancing crack tip.
- 2) Delamination with quite a considerable amount of unbuckled filmstrip left behind the advancing crack tip.
- 3) Similar to the above condition, but with allowance for the buckling of the narrow strip.

The strain energy release rate, G is expressed as:

$$G = \frac{(1 - \nu_f^2) h}{2E_f} \sigma_{Tr}^2 \quad (70),$$

where σ_{Tr} is the total radial component of the various stresses and the value of this stress is depends on the type of the model used as shown in Figure 17.

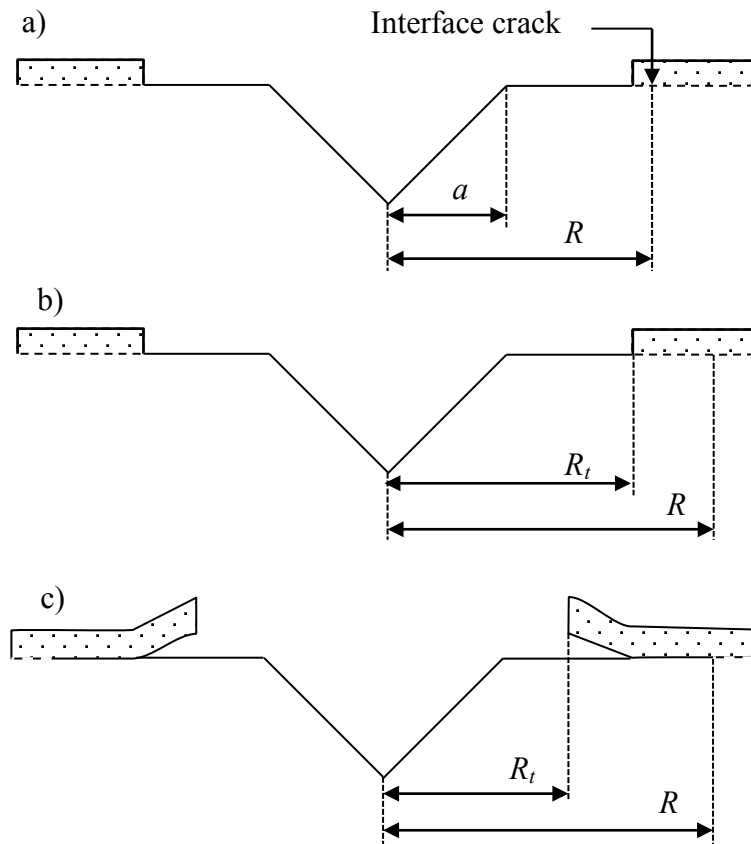


Figure 17. Types of delamination. a) delamination with only a very small strip of film left behind the advancing crack tip b) delamination with quite a considerable amount of filmstrip left behind the advancing crack tip c) similar to the previous condition, but with allowance for the buckling of the narrow strip. Adapted from [59].

3.2 Stresses in Thin Films

There are three main sources of stresses in thin films [61]. They are as follows:

- 1) Epitaxial Stresses;
- 2) Thermal Stresses;
- 3) Intrinsic stresses.

Epitaxial strain is produced due to the difference in the lattice parameters of the thin film and substrate. The corresponding epitaxial stress, σ_E , can be expressed as:

$$\sigma_E = E_f \frac{a_f - a_s}{a_s} \quad (71),$$

where a_f , a_s are the lattice parameters of the film and the substrate, and E_f is the Young's modulus of the film.

Thermal stresses, σ_T , develop when the film/substrate pair is subjected to a temperature change. This is due to the difference in thermal expansions of the substrate and the film. Thin film coatings are usually deposited at temperatures higher than their working temperatures. This leads to development of thermal stress, σ_T , which can be expressed as:

$$\sigma_T = E_f (\alpha_f - \alpha_s) \Delta T \quad (72),$$

where α_f , α_s are the linear thermal expansion coefficients of the film and substrate and ΔT is the difference between the film deposition temperature and the working temperature. There is a strong suggestion of the presence of thermal stresses in case of Ge film over Ni substrate due to the fact that the thermal expansion coefficient of Ge and Ni are $6.1 \times 10^{-6} \text{ m m}^{-1} \text{ K}^{-1}$ and $13 \times 10^{-6} \text{ m m}^{-1} \text{ K}^{-1}$ respectively [48].

The non-equilibrium conditions that exist during deposition and growth of thin film coatings are the fundamental cause for the formation of intrinsic stresses. There are various sources for the intrinsic stress in films, like consolidation of grain boundaries, grain growth, presence of impurities in the film and development of surface stresses.

3.3 Residual Stress Measurements

Thin film coatings on substrate are mostly in a state of residual stress and the various sources for this stress have been discussed above. Wafer curvature method is the most commonly used technique to estimate the amount residual in thin films. Stoney in his 1909 paper [62]

demonstrated that for a pre-stressed film over a thick substrate, the average stress in the film could be related to the curvature of the substrate, which can be expressed as:

$$\sigma_f = \frac{E_s h_s^2}{6(1-\nu_s)h_f} \kappa \quad (73),$$

where E_s , ν_s are the Young's modulus and Poisson's ratio of the substrate, h_s , h_f are the thickness of the film and the substrate and κ is the difference in curvature of the substrate before and after the deposition of the film.

The wafer curvature method [63 - 64] works by measuring the difference in the radius of curvature of the substrate before and after deposition of the thin film. The nature and the extent of curvature are measured using a surface profileometer, or a laser beam. Convex curvature of the substrate suggests that the film is in a state of biaxial compressive stress and concave curvature suggests that the film has a biaxial tensile stress.

The Stoney relation for average stress measurement is valid only when the film and substrate are completely homogeneous and isotropic. The thickness of the film and substrate is uniform, and when the stresses in films are equi-biaxial. However in practical situations, not all these conditions are met. This may lead to a substantial amount of error in the estimated stress values. One method to overcome this problem is by applying the Stoney formula pointwise and obtaining the local stresses. Recent works [61, 65 - 66] have developed the solutions, which are extensions of the original Stoney formula but with reduced constraints.

CHAPTER 4:

ADHESION MEASUREMENT AND DISCUSSIONS

4.1 Adhesion Measurements

When all other factors that affect the cycle life of the electrode are similar, the electrochemical performance of the electrode depends primarily on the adhesion between the thin film Ge electrode and Ni current collector. Thus, it is of primary importance to measure and quantify the adhesion between the electrode and the current collector. The claim that ion beam modification improves the adhesion strength is tested and quantified in this study.

There is also a need to quantify the effect of atomic level intermixing produced by ion beam irradiation, on the adhesion of Ge thin film over Ni current collector. The nanoindentation and the superlayer indentation tests were used in this study to evaluate the adhesion of Ge thin film anodes over Ni current collector and to analyze the effect of ion beam irradiation on the adhesion properties. The schematics of the samples used for the nanoindentation and the superlayer indentation tests are shown in Figure 18.

4.2 Fabrication of the Test Specimens

Four Ge film over Ni substrate samples were fabricated at the University of Florida. First all the four electrode samples were fabricated by depositing a thin film of Ge with a thickness of 140 nm over a 0.001 in. thick Ni substrate. This deposition was done using electron beam evaporation. The deposition process was conducted at room temperature and Ge thin film was deposited at a rate of 0.5 nm s^{-1} over the Ni substrate. Next, two of these fabricated electrodes were ion beam irradiated by self-implanting the Ge film with Ge^+ ions having an energy of 260

keV, a dose of $1 \times 10^{16} \text{ cm}^{-2}$ at 77 K. HR-TEM results showed that this irradiation resulted in an ion beam mixing of 5 nm [12, 32]. A highly compressive W superlayer was then deposited on one of the as-deposited sample and one of the ion beam irradiated samples.

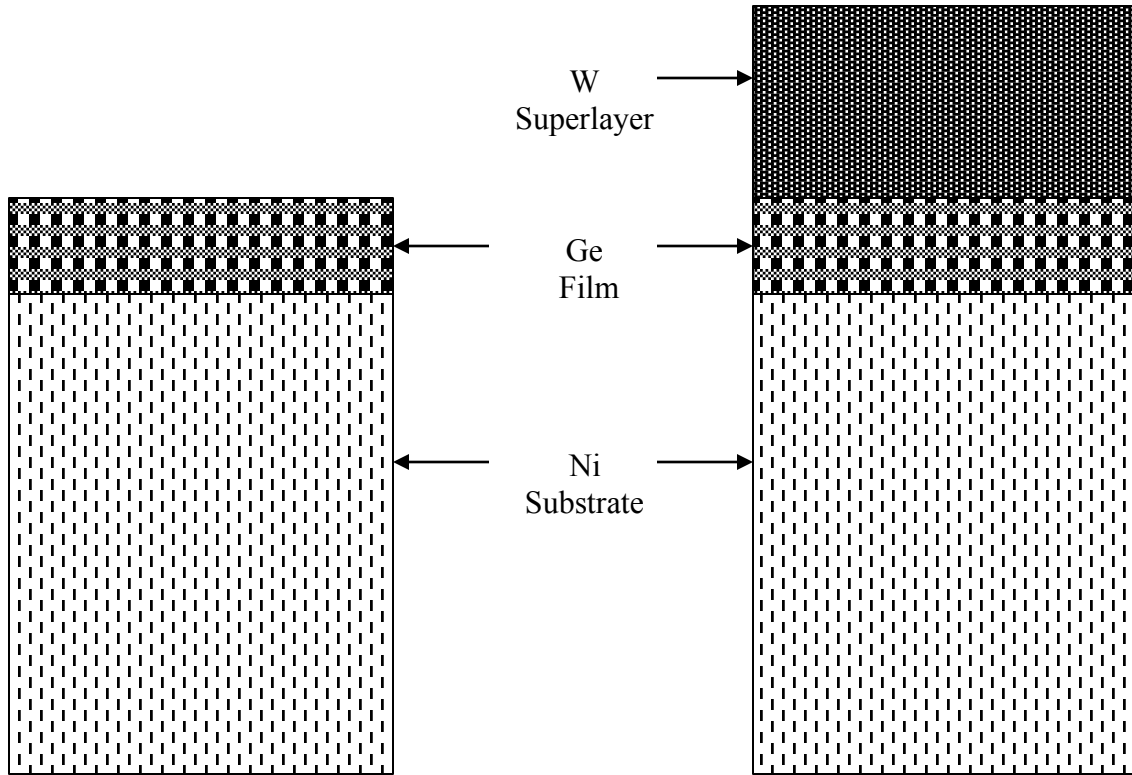


Figure 18. Schematics of the indentation test and the superlayer indentation test specimens.

4.3 Load Range Selection

Generally, indentation depths close to the film thickness are enough to produce delamination of the thin film from the substrate. However, in case of a brittle film over a ductile substrate, there are no signs of delamination when the indentation depth is in the range of the film thickness. In such a case, there is a need for indentation depths that are much deeper than the thickness of the film. In our study, all tests were performed using the Hysitron Tiboindenter® fitted with a diamond cono-spherical tip, which has a tip radius of 1 μm . The indenter was

operated in the load control mode with a constant loading rate. The range of loads that were applied on each sample for the adhesion measurements was determined by a train and error method. It was observed that when the applied load was below a certain value, no signs of delamination were evident when the specimen was viewed under an optical microscope. Increasing the applied loads beyond a certain limit had little effect on the measured G values. According to this criterion, a range of loads between 50 mN to 500 mN in 50 mN increments was applied on the four samples. The various load-displacement curves for the as-deposited sample with no W superlayer are shown in Figure 19.

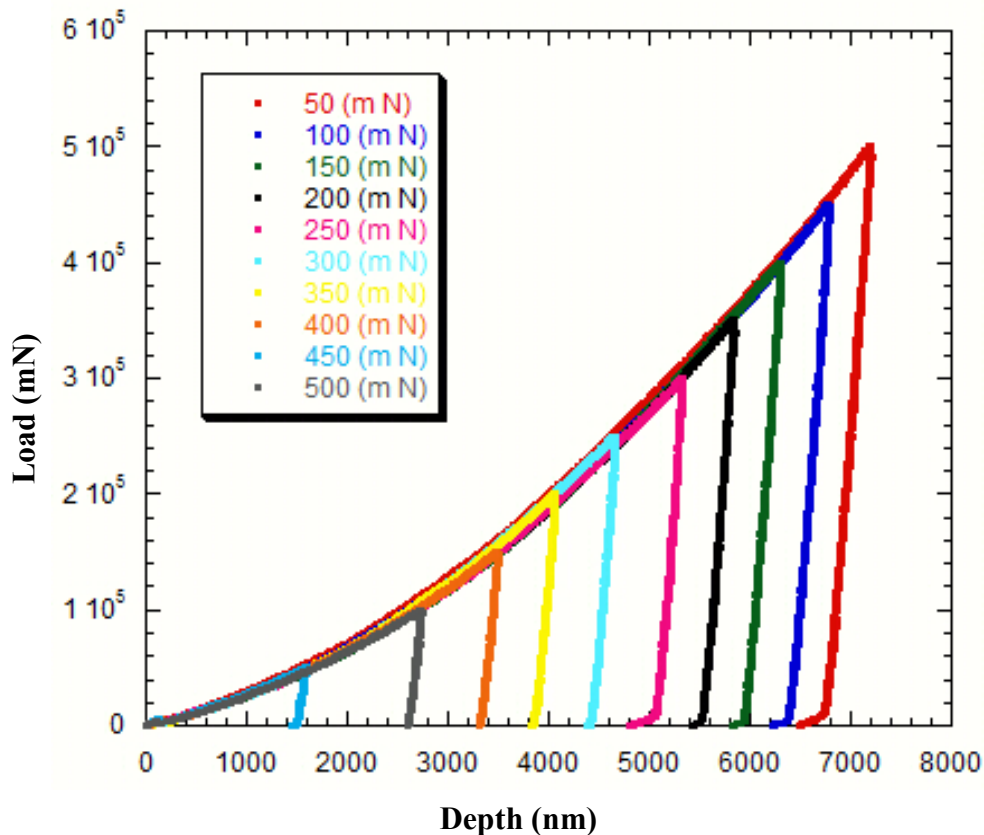


Figure 19. Load-displacement curves for the non-irradiated sample without superlayer.

The strain energy release rate is calculated only for very small and specific distances around the point of indentation. Therefore, there are chances that the measured strain energy release rate may not accurately depict the strain energy release rate of the entire coating. This effect maybe due to a variety of reasons, like difference in surface roughness, minute variation in the coating thickness, impurities in the coating and variance in atomic level intermixing. To account for these variances six sets of indents were performed at various locations on each sample. Each set consisted of ten indents spaced $100\ \mu\text{m}$ from each other and each row of indents was separated by $200\ \mu\text{m}$. The schematics of this arrangement of indents are shown in Figure 20.

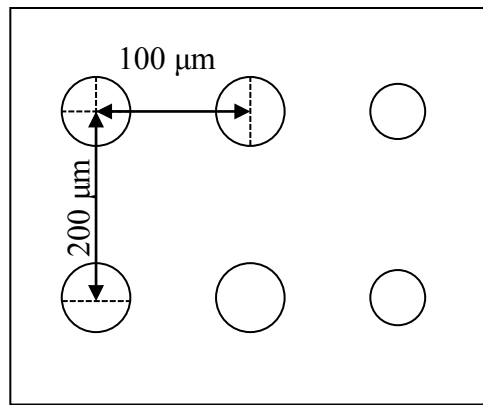


Figure 20. Spacing between each indent and each set of indents.

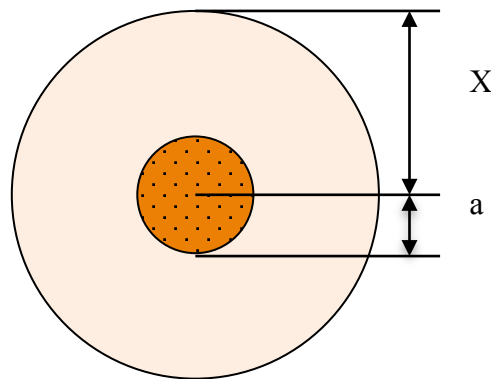


Figure 21. Schematic of delamination measurement.

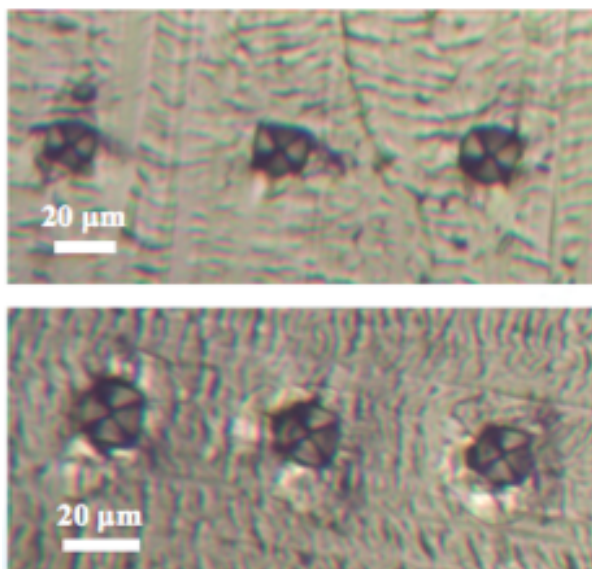


Figure 22. Delaminations observed in non-irradiated and irradiated samples.

The radii of various delaminations, produced by the process of indentation, were measured using an optical microscope and a micron ruler. The delamination radius measurement schematics and delaminations of irradiated and non-irradiated samples are shown in Figures 21 and 22.

4.4 Analysis of the Test Data

In our study, the adhesion of the Ge thin film over the Ni substrate is tested using qualitative and quantitative analysis. The inadequacy of the Marshall and Evans indentation model and the need for an alternative model in case of a brittle on ductile substrate is discussed in the following sections.

4.4.1 Qualitative Analysis

The adhesion strength of the irradiated and non-irradiated samples was qualitatively estimated by means of excursions or pop-in features in the load-displacement curves. Excursions are characterized by a sudden increase in depth without any increase in the load when specimens are loaded in load control, and a sudden drop in load without any change in displacement in the

case of displacement control experiment. The load-displacement curves of the samples with and without the superlayer are shown in Figures 23 and 24.

The occurrence of first pop-in feature in the load displacement curve marks the transition from pure elastic loading to elastic-plastic loading. In ductile materials, this excursion serves as a good indication of the material's yield point. In case of a brittle material, the pop-in phenomenon is a strong indicator of development of radial cracks. They also suggest the fracture of thin film coatings. The energy released for the formation of these cracks can be calculated from the difference in energy before and after the formation of cracks.

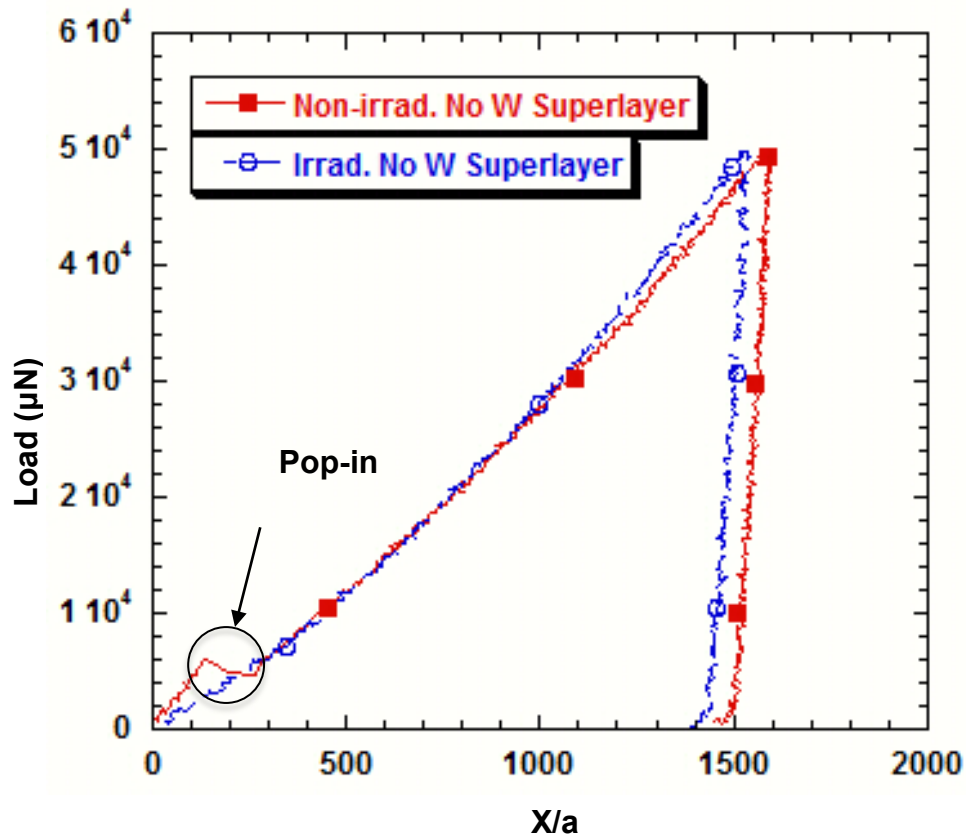


Figure 23. Pop-in observed in non-irradiated samples without the superlayer.

The excursion or pop-in feature appears distinctly only in the case of non-ion beam irradiated samples at indentation depths equal to the thickness of the Ge film coatings in case of

the sample without the superlayer and at indentation depths equal to that of the bilayer thickness in case of samples with the superlayer. Microscopy images of the non-ion beam irradiated samples confirmed the formation of radial cracks as suggested by the excursion features. The presence of excursions strongly suggested a fracture of the Ge films in the non-ion beam irradiated samples and absence of such extrusion features in ion beam mixed samples suggested that the ion beam irradiated coatings survived without cracking. Thus, the extrusion features help to confirm that the adhesion of ion beam mixed samples is higher than the non-ion beam irradiated samples.

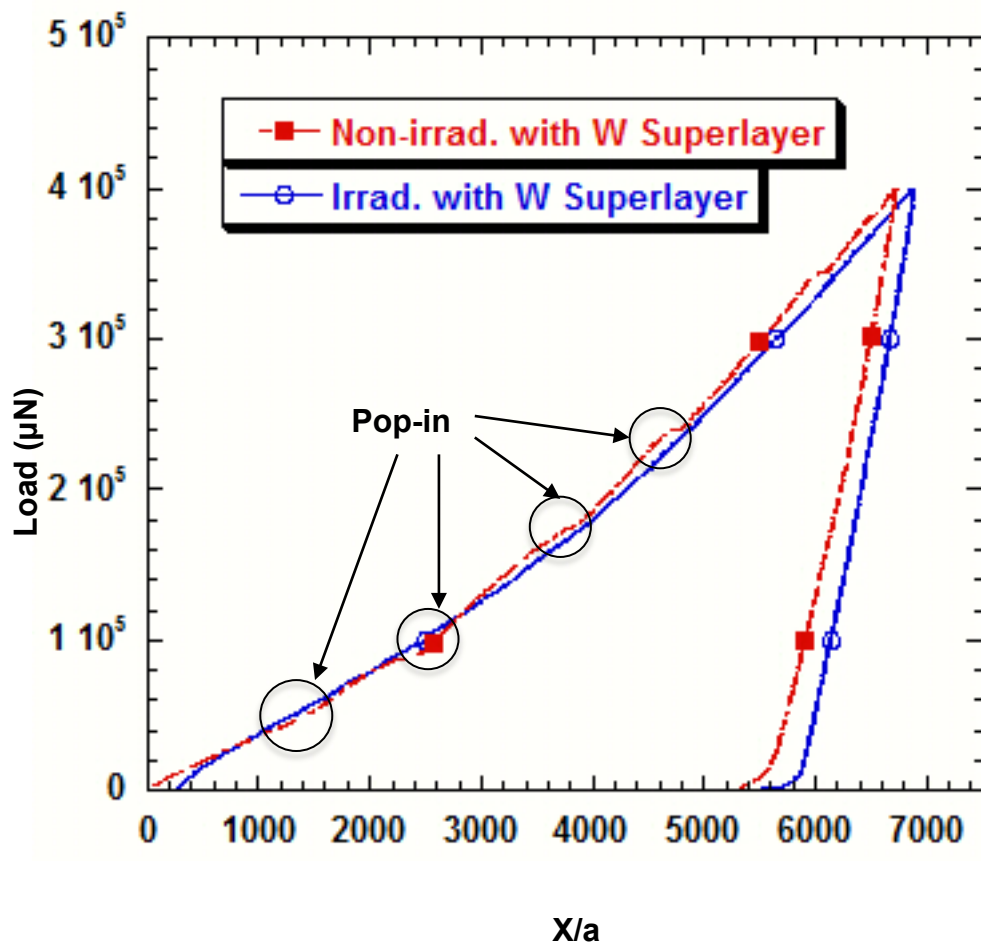


Figure 24. Pop-in observed in non-irradiated samples with W the superlayer.

Micro pop-in features were also observed at indentation depths much greater than the film and the bilayer thickness. Due to the ductile substrate used in this study, the occurrence of these micro pop-in events strongly suggests the large-scale plastic deformation of the substrate, around the indenter tip.

It was observed that the indentation-load required to delaminate the Ge film from the Ni substrate was much higher in case of irradiated samples compared with the non-irradiated samples.

4.4.2 Quantitative Analysis

Initially, the Marshall and Evans model was used to quantify the adhesion of Ge film over the Ni substrate. However, the model produced extremely high and unreasonable adhesion values.

Since the material parameters and the geometry of the specimens are known, the depth of indentation and the radius of delamination are the two parameters that were measured to estimate the adhesion of the interface, using this model. The depth of indentation was measured from the load-displacement curves and the radius of delamination was measured using light microscopy. The Marshall and Evans model works well for the extraction of strain energy release rate values when the indentation depth is similar to the thickness of the film layer or the bilayer thickness in case of the superlayer test. However, once the depth of indentation is much higher than the film thickness, large-scale plastic pile-up starts occurring around the indenter tip. The unreasonably high G values produced by the Marshall and Evans model were due to the fact that the model does not account for the substrate effects that occur at indentation depths much higher than the film thickness. Due to this drawback, this model could not be used for our analysis. The values of the energy release rate calculated using this model are show in Table 1.

Table 1. Strain energy release rate values of the irradiated and non-irradiated samples with W superlayer.

Sample type	Indentation depth (μm)	Crack radius (μm)	Strain energy release rate, G (J/m^2)
Non-irradiated	6.94	27.3	8.8×10^4
Irradiated	6.63	15.2	64.4×10^4

The inadequacy of the Marshall and Evans model led us to use the Drory and Hutchinson model to estimate the energy release rate values of the irradiated and non-irradiated samples. In this model, the radius of indentation, a and the delamination radius, X , are the two parameters that were measured for the estimation of the strain energy release rate values of the interface as the material properties, geometry and the stresses in the specimen were known. In order to calculate the strains produced by the intrinsic and the indentation stresses, in the tangential and radial directions, the displacements are first calculated. This was calculated by solving equation (64), which lead to following expressions:

$$\frac{du}{dr} = \left[b_1 + 2b_2 \left(\frac{r}{a} \right) + 3b_3 \left(\frac{r}{a} \right)^2 \right] e^C \quad \frac{u}{r} = \left(\frac{a}{r} \right) e^C \quad (74),$$

$$C = \left[b_0 + b_1 \left(\frac{r}{a} \right) + b_2 \left(\frac{r}{a} \right)^2 + b_3 \left(\frac{r}{a} \right)^3 \right]$$

where the values of b_0 , b_1 , b_2 , and b_3 were calculated based on the strain hardening rate and the Young's modulus to yield strength ratio (E/Y) of the substrate [59].

For the type A model, σ_{Tr} in equation (70) is the sum of the residual intrinsic stresses, σ_0 and the radial component of the indenter stress, σ_r ($\sigma_{Tr} = \sigma_0 + \sigma_r$). The total radial components of the stress at any point were calculated using the respective strains in the radial and tangential direction. Once the σ_{Tr} is known, the value of the strain energy release rate is obtained by substituting the value of σ_{Tr} in equation (70).

Based on the relationship between the strain energy and the ratio of indentation radius to radial displacement, it is clear that the strains produced by the indenter have a larger effect when the displacements are almost twice the radius of indentation. The strains produced by the indenter are compressive in nature. When the displacements are between $2a$ and $3a$, the trend of strain energy per unit area depends on the nature of residual stress present in the thin film coating. If compressive stresses are present, the strains due to the intrinsic stress and the compressive strain due to the indenter add up. Thus, U values gradually decrease and eventually reach the monotonic value of U_0 . This has been the case in our study. However, if intrinsic tensile stresses are present in the film, the strains produced by these stresses are tensile and strains due to indentation are compressive. Thus, the value of U follows a decreasing pattern and falls well below U_0 before reaching a steady state U_0 value.

The variance of the strain energy release rate with respect to the ratio of the delamination radius, X , to the radius of contact, a , for all the four sample are shown in Figures 25, 26. It was observed that the energy release rate values depended primarily on the indentation-induced stresses at low X/a ratios, but this dependence was seen to decrease with increase in the X/a ratio. When the delamination radius reached $2.5a - 3a$, the dependence of G values on indentation stresses were substantially reduced. The intrinsic residual σ_0 stresses were observed to be the primary contributor to the G values in this range.

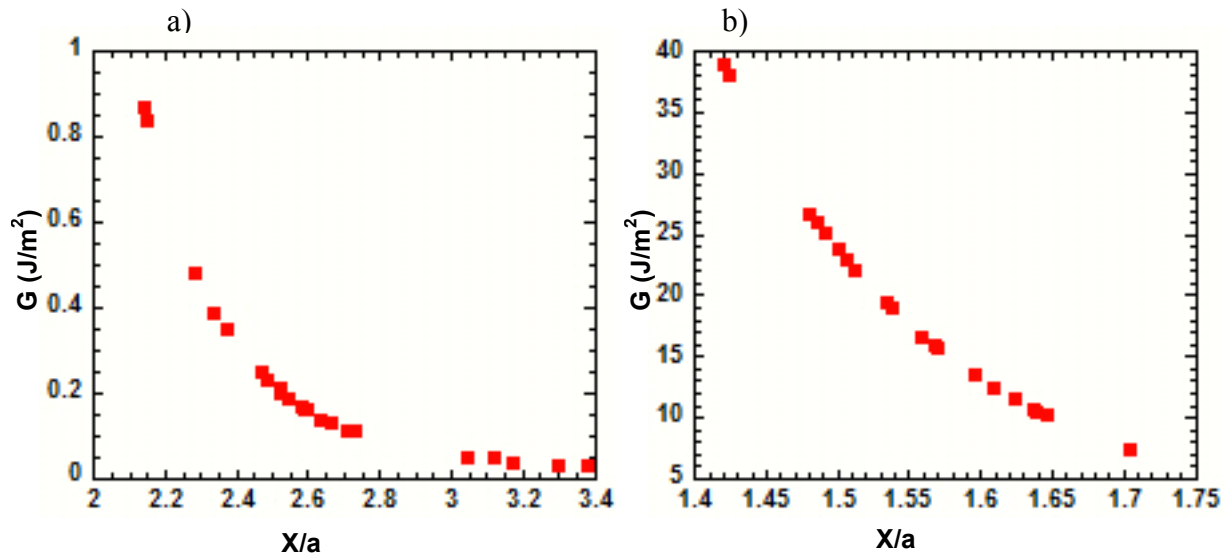


Figure 25. G vs. X/a values for a) as-is and b) irradiated samples with no W superlayer.

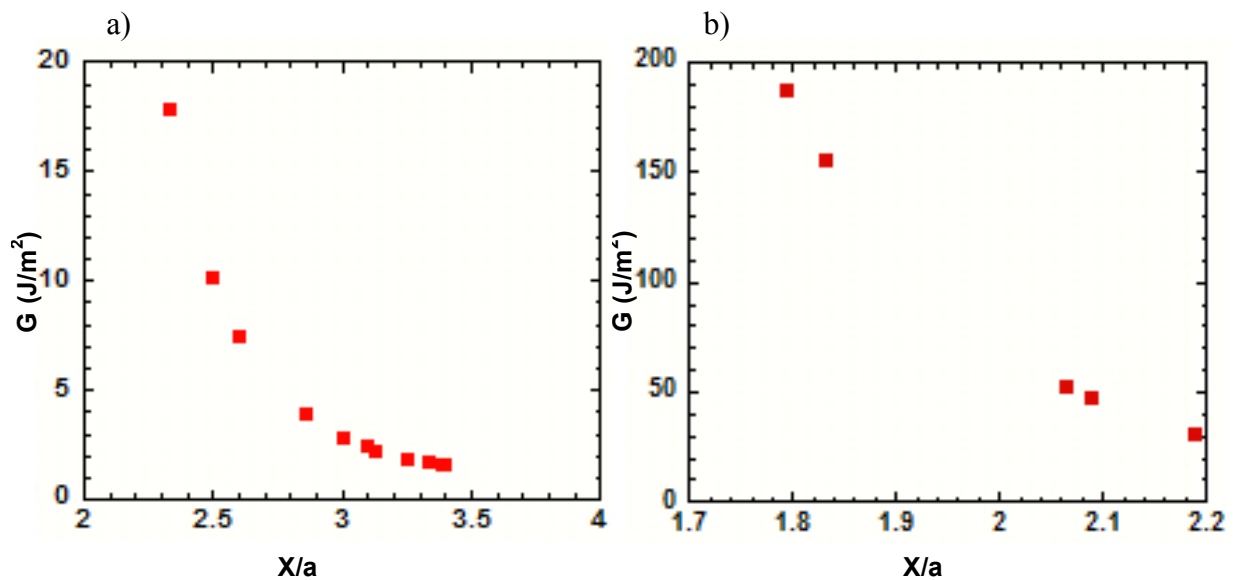


Figure 26. G vs. X/a values for the a) as-is and b) irradiated samples with the W superlayer.

It is interesting to note that the value of the energy release rate rapidly decreases as the X/a ratio increases. However, once the delamination radius was equal to $2.5a - 3a$, the G values steadily started approaching the G_0 values. Another observation was that how the radius of

delamination X for the majority of the indents in each of the four samples fell within a specific range, listed in Table 2. The strain energy release rate values corresponding to the maximum applied load for all the four samples are listed in Table 3.

Table 2. Range of delamination radius.

Sample	The range of delamination radius, X
As-is no superlayer	2.40a - 3.40a
Irradiated, no superlayer	1.45a - 1.65a
As-is with W superlayer	2.50a - 3.40a
Irradiated with W superlayer	2.00a - 2.20a

Table 3. Strain energy release rate for irradiated and non-irradiated samples.

Sample	Max. Load (mN)	X/a	G (J/m ²)
AsIs No Superlayer	500	2.52	0.21
Irradiated No Superlayer	500	1.63	10.56
AsIs with W Superlayer	500	3.10	5.98
Irradiated with W Superlayer	500	2.06	52.16

From the analysis of the strain energy release rate values and delamination radius trends, it was observed that there was hardly any delamination when the delamination radius is less than twice the indentation radius.

Although the G values estimated by this model may be a slight over estimate due to the development of radial cracks, they could still be used, as the error is not unreasonably high when compared with the Marshall and Evans model. This model suggests that failure at the interface is due to the in-plane shear stresses and the measured toughness values should be considered as mode II fracture toughness. It was observed that the measured G values were much higher than the respective G_0 values for each sample. The deformations of the ductile substrate could be the reason for such high G values. Another interesting observation was that the G values of the interface were also much larger than the toughness of the film. This observation agrees well with previous adhesion studies of thin brittle films under a state of compression over ductile substrates. For such cases, it was observed that even when the toughness of the interface is greater than the toughness of the film; the interface still remained as the preferred path for crack propagation.

To conclude, the adhesion of the ion beam irradiated samples was qualitatively shown to be higher than for the non-irradiated ones. Quantitate results have shown that the adhesion values of the irradiated samples were approximately one of order magnitude higher than of the non-irradiated samples.

CHAPTER 5: SUMMARY AND FUTURE WORKS

5.1 Summary

In this study, the adhesion of Ge thin film electrodes over Ni current collector, which have been used as alternative anodes for Li ion batteries, were analyzed. The adhesion values were measured using nanoindentation and the superlayer indentation techniques. The results from this study have qualitatively shown that ion beam modified electrodes produced by irradiation have better adhesion properties than the non-irradiated electrodes. Quantitatively, the study had shown that the process of ion beam mixing improved the adhesion of Ge on Ni up to one order of magnitude.

To quantify the adhesion of Ge films over Ni substrate, the strain energy release rate was initially estimated using the Marshall and Evans model. However, the G values estimated using this model were extremely high and unrealistic. It was later concluded that this model was capable of producing reasonable G values only when the indentation depth was less than or close to the thickness of the film. In case of this study, which involved a ductile substrate, indentation depths in the range of the film thickness did not produce any delamination. Hence there was a need for indentation depths much greater than the film thickness. The Marshall and Evans model does not work well when the indentation depth is much greater than the film thickness, as it does not account for the substrate plastic deformation produced at large indentation depths. This limitation of the Marshall and Evans model, lead to the use the Hutchinson model for the estimation of the strain energy release rate values.

5.2 Suggestions and Future Work

5.2.1 Surface Roughness

The surface of the sample was rough and this led to problems in the estimation of the radius of delamination. As a result, the delamination radius of samples was examined using a variety of optical microscopes, which had different filters. To get a better estimate of radius of delamination, the delaminated portion of the film could be detached from the bulk of the film by indenting the film with very small load, such that the indentation depth is around half of the coating thicknesses. During this process, care must be taken, since deeper indentations may cause further growth of the interface crack. Acoustic emission microscopy could also be used for the estimation of the radius of delamination.

5.2.2 Effect of the Ion Dose

Ion beam irradiation produces the transition of crystalline Ge (c-Ge) to amorphous Ge (α -Ge) and nanostructured Ge [19, 21, 27]. Irradiation also produces various levels of intermixing of Ge film with the Ni substrate [12]. Thus, the effect of irradiation dose on the adhesion of Ge thin film electrode to the current collector could also be studied.

5.2.3 Plane Strain Indentation

The strain energy release rate values could be measured by using a plane-strain wedge indenter and the Vlassak's model [58]. As the wedge indenter loads the crack in a plane-strain fashion, the hoop stresses that generally accompany radial displacement could be avoided. The elimination of these hoop stresses would result in a more accurate estimation of adhesion values.

5.2.4 Environmental Considerations

The working environment of the anode inside the Li ion battery is much different than the environment in which the adhesion studies were conducted. Higher temperatures, constant

exposure to moist environment and pH of the electrolyte used in the battery may all have an effect on the adhesion properties of the thin film electrode over the current collector [1 - 4].

It is known that interface problems are multimodal in nature. Although the Hutchinson model gives a good estimate of the strain energy release rate, it does not have a provision to measure the phase angle of the interface crack. A finite element model could be developed to understand the ratio of the shear to tensile stresses at the interface. This is due to the fact the analytical solution for the phase angle ahead of the crack developed in previous studies [67] may not work well for this condition due to the large-scale plastic deformation.

REFERENCES

- [1] K. Matsuki and K. Ozawa, “General Concepts,” in *Lithium Ion Rechargeable Batteries*, K. Ozawa, Ed. Wiley-VCH Verlag GmbH & Co. KGaA, 2009, pp. 1–9.
- [2] Y.-M. Chiang, “Building a better battery,” *Science(Washington)*, vol. 330, no. 6010, pp. 1485–1486, 2010.
- [3] M. Armand and J.-M. Tarascon, “Building better batteries,” *Nature*, vol. 451, no. 7179, pp. 652–657, 2008.
- [4] M. J. Armstrong, C. O’Dwyer, W. J. Macklin, and J. D. Holmes, “Evaluating the performance of nanostructured materials as lithium-ion battery electrodes,” *Nano Res.*, vol. 7, no. 1, pp. 1–62, Jan. 2014.
- [5] D. Guyomard and J.-M. Tarascon, “Rocking-chair or lithium-ion rechargeable lithium batteries,” *Adv. Mater.*, vol. 6, no. 5, pp. 408–412, May 1994.
- [6] G. E. Moore, “Cramming More Components Onto Integrated Circuits,” *Proc. IEEE*, vol. 86, no. 1, pp. 82–85, Jan. 1998.
- [7] V. Chabot, S. Farhad, Z. Chen, A. S. Fung, A. Yu, and F. Hamdullahpur, “Effect of electrode physical and chemical properties on lithium-ion battery performance: Energy storage,” *Int. J. Energy Res.*, vol. 37, no. 14, pp. 1723–1736, Nov. 2013.
- [8] R. A. Huggins and W. D. Nix, “Decrepitation model for capacity loss during cycling of alloys in rechargeable electrochemical systems,” *Ionics*, vol. 6, no. 1–2, pp. 57–63, 2000.
- [9] R. A. Huggins and D. Elwell, “Morphological stability of a Plane interface during electroncrystallization from molten salts,” *J. Cryst. Growth*, vol. 37, no. 2, pp. 159–162, 1977.
- [10] E. Peled, “The Electrochemical Behavior of Alkali and Alkaline Earth Metals in Nonaqueous Battery Systems—The Solid Electrolyte Interphase Model,” *J. Electrochem. Soc.*, vol. 126, no. 12, pp. 2047–2051, Dec. 1979.
- [11] M. Wakihara and O. Yamamoto, *Lithium Ion Batteries: Fundamentals and Performance*. John Wiley & Sons, 2008.

- [12] N. G. Rudawski, B. R. Yates, M. R. Holzworth, K. S. Jones, R. G. Elliman, and A. A. Volinsky, "Ion beam-mixed Ge electrodes for high capacity Li rechargeable batteries," *J. Power Sources*, vol. 223, pp. 336–340, Feb. 2013.
- [13] J. Graetz, C. C. Ahn, R. Yazami, and B. Fultz, "Nanocrystalline and Thin Film Germanium Electrodes with High Lithium Capacity and High Rate Capabilities," *J. Electrochem. Soc.*, vol. 151, no. 5, p. A698, 2004.
- [14] A. Arico, P. Bruce, B. Scrosati, J. Tarascon, and W. Van Schalkwijk, "Nanostructured materials for advanced energy conversion and storage devices," *Nat. Mater.*, vol. 4, no. 5, pp. 366–377, May 2005.
- [15] M.-K. Song, S. Park, F. M. Alamgir, J. Cho, and M. Liu, "Nanostructured electrodes for lithium-ion and lithium-air batteries: the latest developments, challenges, and perspectives," *Mater. Sci. Eng. R Rep.*, vol. 72, no. 11, pp. 203–252, Nov. 2011.
- [16] G. Impellizzeri, S. Mirabella, and M. G. Grimaldi, "Ion implantation damage and crystalline-amorphous transition in Ge," *Appl. Phys. A*, vol. 103, no. 2, pp. 323–328, Nov. 2010.
- [17] C. S. Fuller and J. C. Severiens, "Mobility of impurity ions in germanium and silicon," *Phys. Rev.*, vol. 96, no. 1, p. 21, 1954.
- [18] B. Laforge, L. Levan-Jodin, R. Salot, and A. Billard, "Study of Germanium as Electrode in Thin-Film Battery," *J. Electrochem. Soc.*, vol. 155, no. 2, p. A181, 2008.
- [19] B. L. Darby, B. R. Yates, N. G. Rudawski, K. S. Jones, A. Kontos, and R. G. Elliman, "Insights for void formation in ion-implanted Ge," *Thin Solid Films*, vol. 519, no. 18, pp. 5962–5965, Jul. 2011.
- [20] H. Huber, W. Assmann, S. A. Karamian, A. Mücklich, W. Prusseit, E. Gazis, R. Grötzschel, M. Kokkoris, E. Kossionidis, H. D. Mieskes, and others, "Void formation in Ge induced by high energy heavy ion irradiation," *Nucl. Instrum. Methods Phys. Res. Sect. B Beam Interact. Mater. At.*, vol. 122, no. 3, pp. 542–546, 1997.
- [21] N. G. Rudawski and K. S. Jones, "Nanostructured germanium prepared via ion beam modification," *J. Mater. Res.*, vol. 28, no. 13, pp. 1633–1645, Jul. 2013.
- [22] E. Holmström, K. Nordlund, and A. Kuronen, "Threshold defect production in germanium determined by density functional theory molecular dynamics simulations," *Phys. Scr.*, vol. 81, no. 3, p. 035601, 2010.
- [23] O. W. Holland, B. R. Appleton, and J. Narayan, "Ion implantation damage and annealing in germanium," *J. Appl. Phys.*, vol. 54, no. 5, pp. 2295–2301, May 1983.

- [24] Y. J. Chen, “Ion implanted nanostructures on Ge(111) surfaces observed by atomic force microscopy,” *J. Vac. Sci. Technol. B Microelectron. Nanometer Struct.*, vol. 15, no. 4, p. 809, Jul. 1997.
- [25] S. G. Mayr and R. S. Averback, “Ion-irradiation-induced stresses and swelling in amorphous Ge thin films,” *Phys. Rev. B*, vol. 71, no. 13, p. 134102, Apr. 2005.
- [26] M. Ghaly, K. Nordlund, and R. S. Averback, “Molecular dynamics investigations of surface damage produced by kiloelectronvolt self-bombardment of solids,” *Philos. Mag. A*, vol. 79, no. 4, pp. 795–820, Apr. 1999.
- [27] P. Bellon, S. J. Chey, J. E. Van Nostrand, M. Ghaly, D. G. Cahill, and R. S. Averback, “Surface damage produced by 20 keV Ga bombardment of Ge (001),” *Surf. Sci.*, vol. 339, no. 1, pp. 135–141, 1995.
- [28] B. R. Yates, B. L. Darby, R. G. Elliman, and K. S. Jones, “Role of nucleation sites on the formation of nanoporous Ge,” *Appl. Phys. Lett.*, vol. 101, no. 13, p. 131907, 2012.
- [29] A. Claverie, S. Koffel, N. Cherkashin, G. Benassayag, and P. Scheiblin, “Amorphization, recrystallization and end of range defects in germanium,” *Thin Solid Films*, vol. 518, no. 9, pp. 2307–2313, Feb. 2010.
- [30] B. Stritzker, R. G. Elliman, and J. Zou, “Self-ion-induced swelling of germanium,” *Nucl. Instrum. Methods Phys. Res. Sect. B Beam Interact. Mater. At.*, vol. 175–177, pp. 193–196, Apr. 2001.
- [31] L. Romano, G. Impellizzeri, M. V. Tomasello, F. Giannazzo, C. Spinella, and M. G. Grimaldi, “Nanostructuring in Ge by self-ion implantation,” *J. Appl. Phys.*, vol. 107, no. 8, p. 084314, 2010.
- [32] N. G. Rudawski, B. L. Darby, B. R. Yates, K. S. Jones, R. G. Elliman, and A. A. Volinsky, “Nanostructured ion beam-modified Ge films for high capacity Li ion battery anodes,” *Appl. Phys. Lett.*, vol. 100, no. 8, p. 083111, 2012.
- [33] M. Ohring, *The materials science of thin films*. Boston: Academic Press, 1992.
- [34] D. E. Packham, “Work of adhesion: contact angles and contact mechanics,” *Int. J. Adhes. Adhes.*, no. 2, pp. 121–128, 1996.
- [35] T. Young, “An Essay on the Cohesion of Fluids,” *Philos. Trans. R. Soc. Lond.*, vol. 95, pp. 65–87, Jan. 1805.
- [36] J. Dundurs and M. Hetényi, “Transmission of force between two semi-infinite solids,” *J. Appl. Mech.*, vol. 32, no. 3, pp. 671–674, 1965.

- [37] E. E. Gdoutos, *Fracture mechanics an introduction*. Dordrecht; Norwell, MA: Springer ; Distributed in North, Central and South America by Springer, 2005.
- [38] J. W. Hutchinson and Z. Suo, “Mixed Mode Cracking in Layered Materials,” in *Advances in Applied Mechanics*, vol. Volume 29, John W. Hutchinson and Theodore Y. Wu, Ed. Elsevier, 1991, pp. 63–191.
- [39] Z. Suo and J. W. Hutchinson, “Interface crack between two elastic layers,” *Int. J. Fract.*, vol. 43, no. 1, pp. 1–18, 1990.
- [40] H. Hertz, “On hardness,” *Verh Ver Beförd. Gewerbe Fleisses*, vol. 61, p. 410, 1882.
- [41] H. HERTZ, “On the contact of solid elastic bodies and on hardness,” *J. Math*, vol. 92, pp. 156–171, 1881.
- [42] Y. Wang and D. Raabe, “Relationship between pile-up and strain-hardening behavior in single crystal indentation testing.”
- [43] G. m. Pharr, W. c. Oliver, and F. r. Brotzen, “On the generality of the relationship among contact stiffness, contact area, and elastic modulus during indentation,” *J. Mater. Res.*, vol. 7, no. 03, pp. 613–617, 1992.
- [44] W. C. Oliver and G. M. Pharr, “An improved technique for determining hardness and elastic modulus using load and displacement sensing indentation experiments,” *J. Mater. Res.*, vol. 7, no. 06, pp. 1564–1583, 1992.
- [45] A. C. Fischer-Cripps, “Critical review of analysis and interpretation of nanoindentation test data,” *Surf. Coat. Technol.*, vol. 200, no. 14–15, pp. 4153–4165, Apr. 2006.
- [46] K. L. Johnson, “The correlation of indentation experiments,” *J. Mech. Phys. Solids*, vol. 18, no. 2, pp. 115–126, 1970.
- [47] A. C. Fischer-Cripps, *Nanoindentation*. Springer Science & Business Media, 2011.
- [48] P. G. Charalambides, H. C. Cao, J. Lund, and A. G. Evans, “Development of a test method for measuring the mixed mode fracture resistance of bimaterial interfaces,” *Mech. Mater.*, vol. 8, no. 4, pp. 269–283, 1990.
- [49] M. P. Hughey, D. J. Morris, R. F. Cook, S. P. Bozeman, B. L. Kelly, S. L. N. Chakravarty, D. P. Harkens, and L. C. Stearns, “Four-point bend adhesion measurements of copper and permalloy systems,” *Eng. Fract. Mech.*, vol. 71, no. 2, pp. 245–261, Jan. 2004.
- [50] R. Shaviv, S. Roham, and P. Woytowitz, “Optimizing the precision of the four-point bend test for the measurement of thin film adhesion,” *Microelectron. Eng.*, vol. 82, no. 2, pp. 99–112, Oct. 2005.

- [51] R. P. Birringer, P. J. Chidester, and R. H. Dauskardt, "High yield four-point bend thin film adhesion testing techniques," *Eng. Fract. Mech.*, vol. 78, no. 12, pp. 2390–2398, Aug. 2011.
- [52] B. Wang and T. Siegmund, "A modified 4-point bend delamination test," *Microelectron. Eng.*, vol. 85, no. 2, pp. 477–485, Feb. 2008.
- [53] A. Bagchi and A. G. Evans, "Thin Film Decohesion and Its Measurement," in *Symposium I – Mechanical Behavior of Diamond and Other Forms of Carbon*, 1995, vol. 383.
- [54] A. Bagchi and A. G. Evans, "Measurements of the debond energy for thin metallization lines on dielectrics," *Thin Solid Films*, vol. 286, no. 1–2, pp. 203–212, Sep. 1996.
- [55] A. Bagchi, G. e. Lucas, Z. Suo, and A. g. Evans, "A new procedure for measuring the decohesion energy for thin ductile films on substrates," *J. Mater. Res.*, vol. 9, no. 07, pp. 1734–1741, 1994.
- [56] D. B. Marshall and A. G. Evans, "Measurement of adherence of residually stressed thin films by indentation. I. Mechanics of interface delamination," *J. Appl. Phys.*, vol. 56, no. 10, pp. 2632–2638, 1984.
- [57] M. D. Kriese, W. W. Gerberich, and N. R. Moody, "Quantitative adhesion measures of multilayer films: Part I. Indentation mechanics," *J. Mater. Res.*, vol. 14, no. 07, pp. 3007–3018, 1999.
- [58] J. J. Vlassak, M. D. Drory, and W. D. Nix, "A simple technique for measuring the adhesion of brittle films to ductile substrates with application to diamond-coated titanium," *J. Mater. Res.*, vol. 12, no. 07, pp. 1900–1910, 1997.
- [59] M. D. Drory and J. W. Hutchinson, "Measurement of the adhesion of a brittle film on a ductile substrate by indentation," *Proc. R. Soc. -Math. Phys. Eng. Sci.*, vol. 452, no. 1953, pp. 2319–2341, Oct. 1996.
- [60] I. SNEDDON, "BOUSSINESQ'S PROBLEM FOR A RIGID CONE," 1948.
- [61] L. B. Freund and S. Suresh, *Thin Film Materials: Stress, Defect Formation and Surface Evolution*. Cambridge University Press, 2004.
- [62] G. G. Stoney, "The tension of metallic films deposited by electrolysis," *Proc. R. Soc. Lond. Ser. Contain. Pap. Math. Phys. Character*, vol. 82, no. 553, pp. 172–175, 1909.
- [63] S. Franssila, *Introduction to Microfabrication*. John Wiley & Sons, 2010.
- [64] M. Pascher, *Analysis of Stresses in Thin Films Imposed by a Wafer Curvature Method*. 2012.

- [65] A. Wikstrom, P. Gudmundson, and S. Suresh, "Analysis of average thermal stresses in passivated metal interconnects," *J. Appl. Phys.*, vol. 86, no. 11, pp. 6088–6095, Dec. 1999.
- [66] T. S. Park and S. Suresh, "Effects of line and passivation geometry on curvature evolution during processing and thermal cycling in copper interconnect lines," *Acta Mater.*, vol. 48, no. 12, pp. 3169–3175, Jul. 2000.
- [67] P. Gu, M. Dao, and R. J. Asaro, "A simplified method for calculating the crack-tip field of functionally graded materials using the domain integral," *J. Appl. Mech.*, vol. 66, no. 1, pp. 101–108, 1999.
- [68] H. Hertz, "On hardness," *Verh Ver Beförd. Gewerbe Fleisses*, vol. 61, p. 410, 1882.
- [69] H. HERTZ, "On the contact of solid elastic bodies and on hardness," *J. Math*, vol. 92, pp. 156–171, 1881.
- [70] A. A. Volinsky, N. R. Moody, and W. W. Gerberich, "Interfacial toughness measurements for thin films on substrates," *Acta Mater.*, vol. 50, no. 3, pp. 441–466, Feb. 2002.

APPENDIX A COPYRIGHT PERMISSIONS

Below is permission for use of Figure 2 and 3.

Order Completed

Thank you very much for your order.

This is a License Agreement between Aadithya Jeyaranjan ("You") and Elsevier ("Elsevier"). The license consists of your order details, the terms and conditions provided by Elsevier, and the [payment terms and conditions](#).

[Get the printable license](#).

License Number	3604940711270
License date	Apr 09, 2015
Licensed content publisher	Elsevier
Licensed content publication	Journal of Power Sources
Licensed content title	Ion beam-mixed Ge electrodes for high capacity Li rechargeable batteries
Licensed content author	N.G. Rudawski,B.R. Yates,M.R. Holzworth,K.S. Jones,R.G. Elliman,A.A. Volinsky
Licensed content date	1 February 2013
Licensed content volume number	223
Licensed content issue number	n/a
Number of pages	5
Type of Use	reuse in a thesis/dissertation
Portion	figures/tables/illustrations
Number of figures/tables/illustrations	2
Format	electronic
Are you the author of this Elsevier article?	No
Will you be translating?	No
Original figure numbers	figures 1,2
Title of your thesis/dissertation	Adhesion of Germanium Electrode on Nickel Substrate for Lithium Ion Battery Applications
Expected completion date	Apr 2015
Estimated size (number of pages)	81
Elsevier VAT number	GB 494 6272 12
Permissions price	0.00 USD
VAT/Local Sales Tax	0.00 USD / 0.00 GBP
Total	0.00 USD

[ORDER MORE...](#)

[CLOSE WINDOW](#)

Copyright © 2015 [Copyright Clearance Center, Inc.](#) All Rights Reserved. [Privacy statement](#). [Terms and Conditions](#).
Comments? We would like to hear from you. E-mail us at customer@copyright.com